15

Design, Development, Dynamic Analysis, and Control of a Pipe Crawling Robot

Amir H. Heidari[1], Mehran Mehrandezh[1], Homayoun Najjaran[2] and Raman Paranjape[1]
[1]*University of Regina, Faculty of Engineering and Applied Science*
[2]*University of British Columbia, School of Engineering*

1. Introduction

Well functioning water networks are essential to the sustainability of a community. Large transmission and distribution water mains are often the most sensitive components of these networks since their failure can be catastrophic. Furthermore, due to the high cost of these pipes, the system does not usually provide redundancy to enable decommission for maintenance and rehabilitation. Hence, failure of such water mains often carries severe consequences including loss of service, severe damages and water contamination. Aging water mains often suffer from corrosion, tuberculation or excessive leakage. These problems can affect water quality and decrease hydraulic capacity of the mains contributing to water loss. In some cases, the main may be structurally weak and prone to breakage.
Prevention and/or early detection of such catastrophic failures need a comprehensive assessment of pipe condition. A proactive inspection approach is critical to the condition assessment as well as cost-effective repair and renewal of water mains. Regular cyclic inspections can provide information on the physical conditions of the pipes and on the rates of material deterioration. Nondestructive/non-intrusive technologies for evaluating pipe condition are essential tools for the early detection. However, more research is required to adapt existing technologies to the unique circumstances of large water mains that cannot be taken off service.
In this context, a robotic pipe crawler as an example of underwater robotic vehicles is designed to carry pipe inspection instruments including Nondestructive Testing (NDT) sensors used for inspection of in-service water mains of different materials. The robot can also provide real-time visual information about the interior surface of the pipe. The visual information and NDT data are synergistically used to make a more reliable decision about the condition of the pipe.
The on-board sensors would serve two purposes, namely (1) provide information for navigation and control of the robot, and (2) collect inspection data that can be post-processed. The proposed system has the following features:

- It remains operational with pipeline in service.
- It has a very simple structure (i.e., the minimum number of moving parts/actuators).
- It is stable enough, throughout its motion, to maximize the performance of the inspection sensors.

- It can suit pipes with inside diameters ranging from 6 to 10 inches.

It also allows for active condition assessment utilizing a variety of NDT methods to monitor defects such as mechanical damage, tuberculation, general wall loss, corrosion pitting, graphitization, cracks, reduced thickness of internal lining, and faulty joints. This can replace the traditional condition assessment methods, namely passive condition assessment, where only historical data are used to estimate the remaining service life of a pipe.

Precise control of the robot motion plays an important role in conducting effective assessment of the pipe condition. Nonlinear friction, backlash in mechanical components and hydrodynamic forces exerted on the robot would require a nonlinear control system design. However, nonlinear system theory is both limited and intricate, so the nonlinear system has to be linearized to take full advantage of linear system theory, which usually requires adjustments once the system departs from the design operating region.

To alleviate this problem, researchers have been recently examining the problem of designing systems that emulate functions of the human cognitive process (Chaudhuri et al., 1996). The challenge of research in this area is to design control systems that are autonomous (self-reliant) and intelligent in the sense that they satisfy the *Turing test* as follows: *if a man and a machine perform the same task and one cannot distinguish between the machine and the human by examining the nature of their performances then the machine is said to be intelligent, otherwise not* (Turing, 1950). Following this criterion some methods based on Artificial Neural Netwrok (ANN) (Hunt et al., 1992), Genetic Algorithms (GA) (Dimeo & Lee, 1995), and Fuzzy Logic (FL) (Lee, 1990) have been proposed in pursuit of modeling and control of nonlinear systems. Among these, FL has achieved increasing attention between control engineers and in industrial systems. The main idea of FL was introduced by Zadeh (Zadeh, 1973), and first applied by Mamdani (Mamdani et al., 1974) in an attempt to control structurally ill-modeled systems. An adaptive fuzzy system is a FL-system equipped with a training algorithm. Conceptually, it is constructed so that the linguistic information from experts can be directly incorporated through fuzzy IF-THEN rules, and numerical information from sensors is incorporated by training the FL-system to match the input-output (I/O) data and reduce the modeling error. However, the perfect match via an adaptive FL-system is generally impossible. Although the stability of an adaptive FL-system has been guaranteed in (Wang, 1994), (Wang, 1993), and (Wang & Mendel, 1992), the modeling error may deteriorate the tracking performance.

In order to improve the performance of the Fuzzy Logic Controller (FLC) and to meet the very basic requirements including stability and robustness, further tuning of the Membership Functions (MFs) and consequent parameters of the rules in Takagi-Sugeno-Kang (TSK) fuzzy systems (Takagi & Sugeno, 1985) is needed which demands optimization techniques and for that matter, incorporating evolutionary algorithms such as ANN and GA. This has led the researchers to introduce novel techniques like ANFIS, NEFCON, NEFCLASS and NEFPROX for this task (Nauck et al., 1997).

The performance of fuzzy controllers depends on two significant issues, namely the soundness of knowledge acquisition techniques and availability of human experts. These two severely restrict the application domains of FLCs. ANFIS bypasses the latter through tuning the FLC directly from a desired I/O data set.

In this context, an Adaptive Neuro-Fuzzy Inference System (ANFIS) (Jang, 1993) was adopted for the velocity servoing of a pipe crawling robot, where the parameters of the ANFIS were optimized based on experts' data obtained via a Human-In-The-Loop (HITL) real-time simulator.

This chapter is organized as follows: in the next section previous research in the field of in-

spection robots and more specifically pipeline inspection robots is reviewed. Next, in section III, the proposed design of the robotic pipe crawler studied in this research is detailed, which is followed by the investigation of kinematics and dynamics of the robot in section IV. Section V elaborates on the controller design for the robotic pipe crawler, including the structure of the controller, details of the human-in-the-loop system exploited in this research, tuning procedure of the controller and also some theoretical background on ANFIS. Simulation and experimental results are depicted and discussed in section VI. Finally, section VII encompasses the conclusion of the accomplished research and suggested future works.

2. Review of Previous Work

2.1 Conventional Inspection Methods

Statistical methods based on the number of pipe breaks per kilometer and reactive inspection techniques such as leak detection have been mainly used in the past for evaluation of water pipe condition. New testing technologies make it possible to develop more efficient and accurate approaches to maintain pipeline integrity through direct inspection. These techniques provide a variety of information about the condition of the pipes depending on their materials. Examples are the number of wires broken in a single section of the Pre-stressed Concrete Cylinder Pipe (PCCP), the depth of corrosion pitting in a ductile iron pipe, the extent of graphitization in a cast-iron pipe, or more generally the presence of leaking water (Grigg, 2006), (Eiswirth et al., 2001) and (Gummow & Eng, 2000).

2.2 Pipeline Inspection Vehicles

Remotely operated or autonomous vehicles moving inside pipes that can deploy NDT equipments have been studied extensively for the past two decades. An exhaustive review of the literature is impossible due to the limited space available. However, various locomotion systems developed and cited in literature for in-pipe operations can be categorized into three main groups as follows:

2.2.1 Pipe Inspection Gauges (PIG)

They are passive devices widely used for inspection of oil pipes and are designed so that sealing elements provide a positive interference with the pipe wall. Once inserted into a line, PIGs are driven through the line by applying pressure in the direction of required movement. A pressure differential is created across the PIG, resulting in movement in the direction of the pressure drop. Upon removal, the information logged using the PIGs onboard data storage unit is played back and analyzed. PIGs are normally employed for the inspection of pipelines with large diameters. Their inspection operations are limited to relatively straight and uninterrupted pipe lines operating in the high-pressure range. Short inspection runs are costly. Besides, the pipeline must be relatively clean for precise inspection.(Shiho et al., 2004),(Nguyen et al., 2001).

2.2.2 Floating Systems/Robots

Autonomous Underwater Vehicles (AUV) and underwater Remotely Operated Vehicles (ROV) are oceanographic locomotion interfaces used for data acquisition in subsea and deepwater missions. The applicability of existing floating robots in the confined environments such as pipes will be very limited. Further modifications will be needed to make them suitable for inspection of pressurized pipelines.(Griffiths, 2003),(Nickols et al., 1997)

2.2.3 Mobile Robots

Significant effort has been put into devising an effective mechanism to drive a robotic system carrying on-board sensors/testing devices through different pipe configurations. The sensors on these robots must be small in physical size, lightweight, and low in power consumption as compared to the other systems mentioned above. Academic researchers and industrial corporations have investigated many variations of drive mechanisms such as wheels, crawlers, wall press, walking, inchworm, screw and pushrods. Some systems have complex mechanisms and linkages, which in turn require complicated actuation and control. Wheeled systems claimed the edge over the majority due to their relative simplicity and ease of navigation and control. Comparatively, they are able to travel relatively fast and far. However, most of the mobile robots developed for this purpose have been residential in research labs because of their lack of ability to move inside pressurized pipes, e.g. (Koji, 1999), (Roh & Choi, 2005), and (Miwa et al., 2002). Some popular variants of mobile robots for pipe inspection are briefly described below.

- **Wheeled/tractor carriers:** These are the simplest drive mechanisms that are targeted for inspecting empty pipes. These remotely controlled vehicles are designed to serve as platforms to carry cameras and navigate through pipes and conduits.
- **Pipe Crawlers:** These are locomotion platforms that crawl slowly inside a pipeline. They can move down the pipeline independent of the product flow and maneuver past the physical barriers that limit inspection. They can even stop for detailed defect assessment. These robots are reconfigurable and can fit pipes with a variety of sizes. (Bradbeer et al., 2000)
- **Helical Pipe Rovers:** The robots developed at the University Libre de Bruxelles are considered as an example of a helical pipe rover (they are called HELI-PIPES). HELI-PIPE family consists of four different types of robots for in-pipe inspection. The robots have two parts articulated with a universal joint. One part (the stator) is guided along the pipe by a set of wheels moving parallel to the axis of the pipe, while the other part (the rotor) is forced to follow a helical motion thanks to tilted wheels rotating about the axis of the pipe. A single motor (with built-in gear reducer) is placed between the two parts (i.e., rotor and stator) to generate the forward motion (no directly actuated wheels needed). All the wheels are mounted on a suspension to accommodate slight changes in pipe diameter and also the curved segments of the pipe. These robots are autonomous and carry their own batteries and radio links. Their performance is, however, limited to very smooth and clean pipes. (Horodinca et al., 2002)
- **Walking Robots:** Wall-climbing robots with pneumatic suction cups and/or electromagnets have been used for inspection of vertical pipes, conduits, and steel structures (Glass et al., 1999). Walking robots are particularly useful for inspection of irregular and rough surfaces.

  Pipe inspection robots can be configured as tethered or wireless. They can be controlled remotely, or being totally autonomous. To the best of our knowledge, all existing pipe rovers are for inspection purposes only. In general, current mobile robotic systems are not yet adequate for on-the-fly repairs in a complex pipe environment.

  Development of the locomotion unit of a robot capable of inspecting in-service pressurized pipes remains a very challenging and novel research topic. Moreover, precise control of such a pipe inspection robot when subjected to flow disturbances necessitates

development of nonlinear control strategies. This study addresses the mechanical design of a pipe crawling robot capable of moving inside pressurized pipes and a fuzzy-logic based control strategy to maintain a constant speed for the robot when moving inside live pipes.

3. The Proposed Design

3.1 Design Factors

Major factors considered in the design of the proposed pipe inspection robot are reviewed in this section. The principle objective put into practice in our design is to build a vehicle to serve as a highly stable platform capable of conducting precise sensing/scanning tasks. The stability of the platform in terms of having smooth motion with regulated cruise speed is necessary for accommodating sensor readings at a high bandwidth. Precise positioning of the vehicle is particularly important for using precision probes to inspect and evaluate the condition of the inner surface of the pipes. The main design requirements of the robot are as follows:

1. The vehicle should be capable of completing inspection without decommissioning the pipeline.
2. The vehicle has to be pressure tolerant up to 20 atmospheres. Freshwater transmission lines are operated at pressures of up to 16 atmospheres, therefore with a reasonable margin of safety we require the vehicle to be able to operate at 20 atmospheres, which corresponds to the hydrostatic pressure experienced at 200 meters of depth in open water.
3. The sensor payload of the vehicle has to be flexible and user interchangeable. The primary use of this vehicle is to carry a number of NDT sensors that are in various states of development. It is therefore necessary for the user to be able to swap and replace sensors within hours.
4. Autonomy of the inspection process:
    a. The length of the survey (several kilometers) makes a tethered vehicle impractical.
    b. Very detailed inspection should be done autonomously.
5. The robot should be designed in a way that it will not deteriorate the sanitation of the drinkable water when used in distribution water pipes.
6. The vehicle should be capable of traveling with any inclined pipe angle. The vehicle shall have the ability to travel vertically, negotiate multiple elbows, and potential obstacles protruding into the pipe up to 1/3 of the pipe diameter.
7. Travel speeds should be a minimum of 3 centimeters per second, with 30 centimeters per second as the desirable speed.
8. Finally, the vehicle should be able to stop and position itself at a specific location within the pipe using its onboard internal sensors, such as optical encoders.

3.2 The Proposed Vehicle Configuration

In our proposed system, we use a low drag cylindrical shape hull as a platform for carrying inspection/navigation sensors and NDT devices. The symmetrical shape of the hull can maintain a laminar boundary layer around the hulls outer surface. The low-drag property of the

main body enables the system to show superior stability against current in the pipe without loosing too much energy which is necessary in minimizing the size of the on-board battery pack required to travel long distances.
The hull consists of the following modules:

- *Nose Module* : This module accommodates a viewport for a digital still or a video camera.
- *Rechargeable Battery Module* : It provides power for propulsion, system hardware, and sensors during mission. The module contains Lithium-Ion rechargeable batteries with a total capacity of 1 *kWh*. The battery module has a built-in charger and can be charged separately from the vehicle as well as in the vehicle.
- *Actuator, Control and Communication Module* : it accommodates the vehicles actuator along with the control and communication electronics. Control instrumentation includes a *3 - axis* magneto-inductive compass, inclinometers, a temperature sensor, and an optical encoder. Communication is done via Bluetooth wireless module for short distances. For distances longer that 30 meters, the controller switches to autonomous operation. The actuator consists of a geared DC motor.

The main hull houses the actuator and the battery pack. The electronics responsible for power conversion, communication to the wireless transceiver, sensor integration, and various electric motor controls is housed in the second module connected to the main hull via a universal joint (see Fig. 1). Further details on the design of the proposed robot can be found in (Ratanasawanya et al., 2006). There is one set of driving wheels located at one end of the hull, pushing

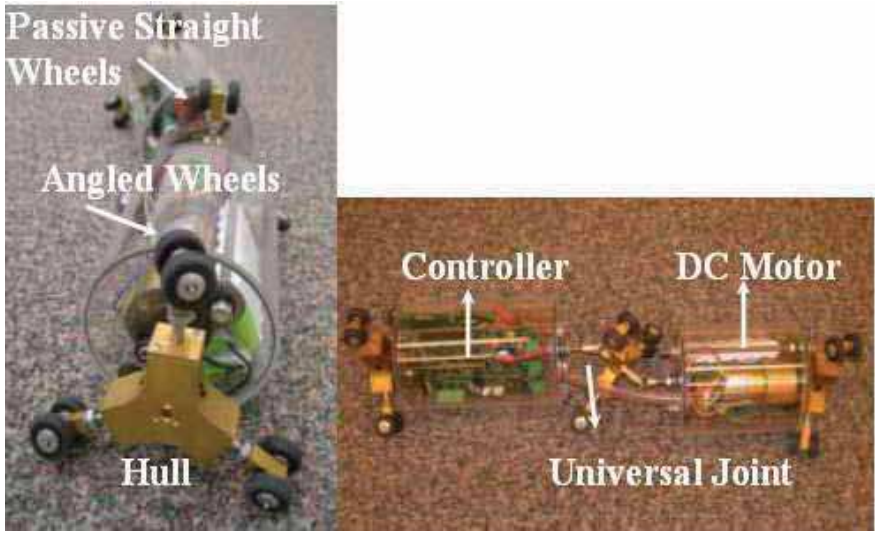

Fig. 1. The pipe inspection robot: (a) active and passive wheels. (b) side view of the robot.

against the pipe inner wall. These wheels are spring-loaded as depicted in Fig. 1. The driving wheels are approximately 4 centimeters in diameter with aluminum hubs and rubber tires. The tires have treads to provide additional traction. Larger compliant tires are appropriate

for bumps and uneven internal surfaces. The driving wheels are actuated by a central geared DC motor which provides forward propulsion for the robot. The on-board electronics will be responsible for producing, filtering and controlling the power delivered to the motor for safe operation. Friction between the passive straight wheels attached to the hulls back end and the pipes wall, prevents the hull from spinning while the main actuator is providing smooth forward motion in the pipe.
Fig. 2 shows a simplified representation of the robots driving mechanism. One should note that,(1) only one pair of driving wheels are considered, and (2) the passive straight back wheels are not shown in this figure for simplicity. As can be seen from Figs. 1 and 2, the driving wheels are positioned at a small angle with respect to the vertical plane of the hull. The wheels are pushed against the inside wall of the pipe and driven along the circumference of the pipe. In this way, they generate a screw-type motion and move along the pipe. This mechanism, as schematically illustrated in Fig. 2, is analogous to a large screw being turned inside the pipe and consequently moving forward. When a reverse driving torque is applied to the wheels, the robot runs backward in the pipe. This design provides simplicity and compactness with minimal blockage of live pipes. Our proposed robot can negotiate pipes composed of straight and curved segments.

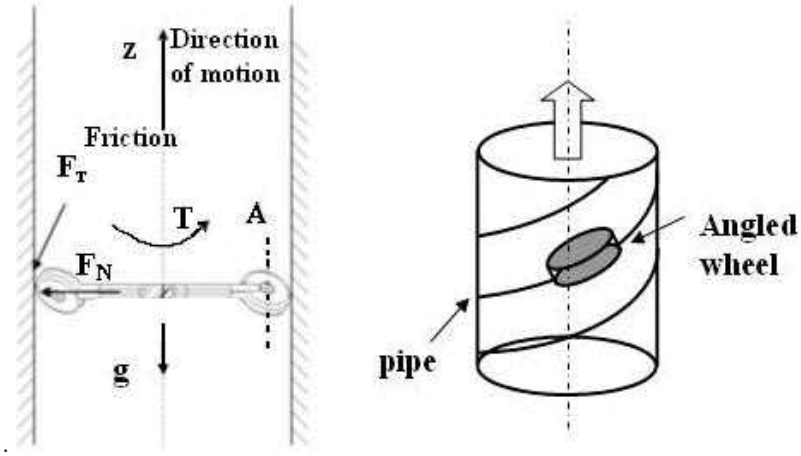

Fig. 2. The drive mechanism of the robot based on the principle of screw.

3.3 On-board Sensors

Three different types of sensors are incorporated into the design, namely (1) navigation, (2) communication, and (3) inspection sensors. However, some sensors potentially can be employed for both navigation and inspection. An optical encoder reading motors shaft displacement was used for localizing the robot inside the pipe. A vision sensor (i.e., a pinhole camera) along with an Omni-directional Stereo Laser Scanner (OSLS) were employed for navigation/inspection purposes. Unbounded position errors due to slippage in wheels is inevitable, therefore the OSLS can be superior over optical encoders to precisely measure lateral translational motion of the robot, namely, sway and two rotational motions, namely pitch and heave,

(Kulpate, 2006). A sensor fusion strategy would be required to integrate orthogonal information coming from different sensing units as the robot moves. It is also noteworthy that some temperature sensors were used in each module to continuously monitor the temperature build up in each water-tight unit.

4. Motion Analysis

In this section the kinematics and dynamics of the proposed robot moving inside a vertical straight pipe are investigated. For simplicity, the dynamic equations are derived based on the following assumptions:

1. The angle of the driving wheels cannot change on the fly;
2. The wheels apply a fixed amount of normal force to the pipe wall preventing the slippage (i.e., no on the fly extension in arms is allowed).

The vehicle model and coordinate systems used in this study are shown in Fig. 3. It is assumed that one DC motor drives the hub and also the wheels attached to the hull (or main body), as the prime actuator. From Fig. 3, frames *i*, *B*, and *W* represent the inertial fixed frame, the body frame attached to the main body of the robot, and the wheel frame attached to the wheel center of rotation, respectively. Physical parameters of the system in the presented dynamic model of the robot and their definition are given in Table 1.

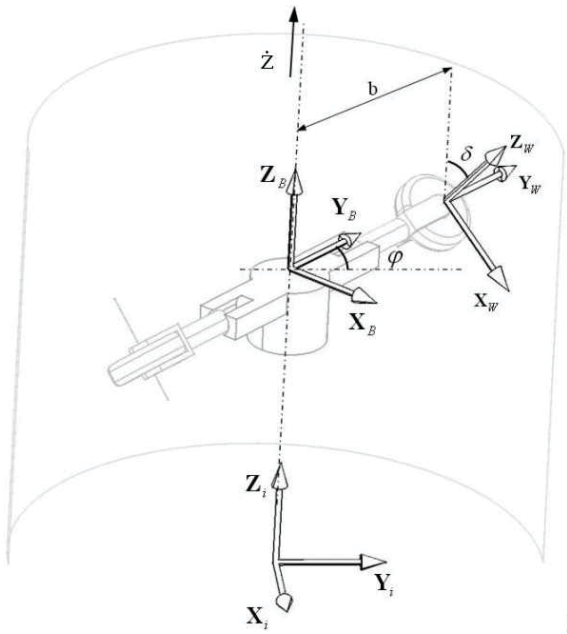

Fig. 3. The simplified model of the robot, with one pair of driving wheels, showing three reference frames.Passive wheels are not shown in this picture.

Physical Properties of the System		
Symbol	Definition	Unit
m	Wheel Mass	kg
M_h	Hull Mass	kg
M_m	Motor Mass	kg
r	Wheel Radius	m
A	Robot's Effective Cross-Sectional Area	m^2
C_d	Drag Coefficient	$-$
μ	Fluid Dynamic Viscosity	$\frac{kg}{m.s}$
ν	Velocity of the Fluid	$\frac{m}{s}$
ρ	Fluid Density	$\frac{kg}{m^3}$
K_f	Damping Constant	$N.m.s$
K_m	Toque Constant	$\frac{N.m}{A}$
K_b	Back EMF Constant	$\frac{N.m}{A}$
R	Motor Resistance	Ω
L	Motor Inductance	H
I_B	Hull Polar Moment of Inertia	$kg.m^2$
I_{WZ},I_{WX}	Wheel Moment of Inertia	$kg.m^2$
I_m	Motor Moment of Inertia	$kg.m^2$
g	Gravitational Acceleration	$\frac{m}{s^2}$

Table 1. Physical Parameters of the Pipe Crawler System

4.1 Robot Kinematics

The infinitesimal translational displacement of the hull COG, dz and the angular displacement of the wheel $d\theta$ can be expressed in terms of the infinitesimal angular displacement of the hull $d\phi$ by:

$$dz = (b + r)d\phi \tan(\delta) \tag{1}$$

$$d\theta = \left(\frac{b + r}{r\cos\delta}\right)d\phi; \qquad \delta \neq \frac{\pi}{2} \tag{2}$$

where δ is the wheel's inclination angle and b denotes the distance between the wheel's center of rotation and that for the hull.

4.2 Robot Dynamics

The dynamic equations of motion of the robotic vehicle can be derived using the standard Lagrangian approach. First we define Lagrangian as:

$$L = T - V \tag{3}$$

where T and V denote the *kinetic energy* and the *potential energy* due to the gravitational forces, respectively. The total kinetic energy of the robotic vehicle can be represented by:

$$T = T_{Motor} + T_{Hull} + \Gamma T_{AW} \tag{4}$$

where T_{Motor}, T_{Hull} and T_{AW} denote kinetic energies of the motor, hull and the angled wheels, respectively, and Γ denotes the number of angled (active) wheels. In (4), the kinetic energy of the passive straight wheels is disregarded. T_{Motor}, T_{Hull} and T_{AW} can be calculated as:

$$\begin{aligned} T_{Motor} &= \tfrac{1}{2} M_m \dot{z}^2 \\ T_{Hull} &= \tfrac{1}{2} M_h \dot{z}^2 + \tfrac{1}{2} I_B \dot{\phi}^2 \\ T_{AW} &= \left\{ (mr^2 + I_{WZ}) \left(\tfrac{bC_\delta}{b+r} \right)^2 + (mr^2 + I_{WX}) S_\delta^2 \right\} \tfrac{\dot{\theta}}{2} \end{aligned} \tag{5}$$

In (5), S_δ and C_δ represent the short form of $\sin(\delta)$ and $\cos(\delta)$, respectively. Considering (1) and (5) the total kinetic energy of the system can be written as:

$$T = \frac{1}{2} \left\{ \left((b+r) \frac{S_\delta}{C_\delta} \right)^2 \alpha_M + \Gamma b^2 \alpha_m + I_B \right\} \dot{\phi}^2 \tag{6}$$

where:

$$\begin{cases} \alpha_M = (M_m + M_h + \Gamma m + \Gamma \frac{I_{WX}}{r^2}) \\ \alpha_m = (m + \frac{I_{WZ}}{r^2}) \end{cases} \tag{7}$$

An infinitesimal change in the potential energy of the robot due to the gravity when moving in a vertical pipe can be calculated as:

$$dV = (M_m + N_h + \Gamma m) g dz \tag{8}$$

After substituting eqn. (1) in (8) one gets:

$$dV = (M_m + M_h + \Gamma m)(b+r) g d\phi \tan(\delta) \tag{9}$$

Considering the angle of rotation of the hull ϕ as the only generalized coordinate in the Lagrange formulation, one can write:

$$\frac{d}{dt} \left(\frac{\partial L}{\partial \dot{\phi}_i} \right) - \frac{\partial L}{\partial \phi} = Q \tag{10}$$

The generalized force Q applied on the robot moving inside the pipe is given by:

$$Q = T_m - T_f - T_D \tag{11}$$

where the right hand side of the above equation represents the non-potential generalized torques such as the electromechanical torque generated by the motor, T_m, the resisting torques due to the friction between the wheels and their axles T_f, and the resisting torque due to hydrodynamic drag force posed on the system T_D all projected onto the generalized coordinate, ϕ.

Friction plays a significant role in creating the motion of the robot. Insufficient friction at the point-of-contact between the wheels and the pipe wall leads to wheel slippage. The slippage constraint of a wheel is expressed as (using Coulomb friction law):

$$F_T \leq \mu F_N \tag{12}$$

where μ denotes the friction coefficient, and F_N denotes the normal force applied on the internal surface of the pipe by the robot's wheels. Therefore, the resisting torque due to the internal friction can be obtained from the following equation:

$$T_f = \Gamma \mu b F_N + K_{f_1}\dot{\phi} + K_{f_2}\dot{\theta} \tag{13}$$

One should note that in (13) :

1. $\Gamma \mu b F_N$ models the *Coulomb friction* applied to the hub acting on the wheels.
2. $K_{f_1}\dot{\phi}$ and $K_{f_2}\dot{\theta}$ model the *viscous friction* on the hub and the wheels, respectively.

From (2), the angular velocities of the hub and the wheels, namely $\dot{\phi}$ and $\dot{\theta}$ are related. Therefore one can write;

$$T_f = \Gamma \mu b F_N + K_f \dot{\phi} \tag{14}$$

where :

$$K_f = K_{f_1} + \frac{b+r}{rC_\delta} K_{f_2} \tag{15}$$

The hydrodynamic drag force induced by the flow on the robot, projected onto the generalized coordinate ϕ, can be expressed as follows:

$$T_D = bS_\delta \frac{\rho C_d A}{2} \Big((b+r)\dot{\phi} S_\delta + \nu \Big)^2 \tag{16}$$

where ρ, A, ν and C_d are as listed in Table 1. One should note that in (16):

1. The effect of the rotational motion of the robot on the drag coefficient is not considered, therefore, the drag coefficient is assumed to remain constant as the robot moves.
2. Drag force on the wheels is negligible.

By substituting (14) and (16) in (11), the generalized force Q will be computed as:

$$Q = T_m - \Gamma \mu b F_N - K_f \dot{\phi} - bS_\delta \frac{\rho C_d A}{2} \Big((b+r)\dot{\theta} S_\delta + \nu \Big)^2 \tag{17}$$

Using (17) and substituting T and V from (6) and (9) into (10), the following closed form solution in form of a nonlinear 2^{nd}-order differential equation for the wheels motion (and correspondingly the robot motion) can be obtained:

$$\ddot{\phi} = \frac{T_m - f(\dot{\phi}, \nu) - a_1}{a_2 + a_3 + I_B} \tag{18}$$

where:

$$\begin{cases} f(\dot{\phi}, \nu) = K_f \dot{\phi} + bS_\delta \frac{\rho C_d A}{2} \Big((b+r)\dot{\phi} S_\delta + \nu \Big)^2 \\ a_1 = \Gamma \mu b F_N + (M_m + M_h + \Gamma m)(b+r) g \tan(\delta) \\ a_2 = (M_m + M_h + \Gamma m + \Gamma \frac{I_{WX}}{r^2}) \Big((b+r)\tan(\delta) \Big)^2 \\ a_3 = (m + \frac{I_{WZ}}{r^2}) \Gamma b^2 \end{cases} \tag{19}$$

From (18), one can realize that the motion of the robot can be controlled by changing parameters such as the wheel inclination, δ the normal force exerted on the pipe wall via the wheels, F_N, and the torque applied to the wheels actuators, T_m. The only control input that can vary on the fly in our design is the motor torque, namely T_m. How to manipulate this torque in order to maintain a constant speed of motion when the robot is subjected to flow disturbances (i.e., variation in the flow speed, ν) will be discussed in section 5.

4.3 Motor Dynamics

The dynamics of a permanent magnet DC motor is represented by :

$$\begin{aligned} T_m &= K_m i_a \\ \frac{di_a}{dt} &= -\frac{R}{L} i_a(t) - \frac{e_b}{L} + \frac{1}{L} v_{app}(t) \\ e_b(t) &= K_b \dot{\phi}(t) \end{aligned} \tag{20}$$

where T_m is the mechanical torque generated by the motor, e_b is the back EMF of the motor and i_a is the armature current. Here v_{app} is the input voltage (i.e., the control variable) and i_a denotes the armature current. In (20) it is assumed that the DC motor is not geared (i.e., direct drive).

5. Controller Design

The primary objective of a controller is to provide appropriate inputs to a plant to obtain some desired output. In this research, the controller strives to balance hydrodynamic forces exerted on the robot due to the flow disturbances while maintaining a constant speed for the robot. Two sets of disturbance models in the form of step and also sinusoidal changes in flow velocity were generated randomly in a simulated environment. The controller tracks the response of the system to its user defined velocity set-point $\dot{Z}_{set}$ and sends a correction command in terms of the input voltage provided to the DC motor actuators.
We compare the behavior of two controllers in this research: a conventional *PID* controller and a fuzzy logic controller (FLC) trained using adaptive network-based fuzzy inference system (ANFIS) algorithm.
ANFIS generates a fuzzy inference system (FIS) that is in essence a complete fuzzy model based on data obtained from an operator through real-time HITL virtual reality simulator to tune the parameters of the FLC. More specifically parameters that define the membership functions on the inputs to the system and those that define the output of our system.

5.1 Servomechanism Problem

The servomechanism problem is one the most elementary problems in the field of automatic control, where it is desired to design a controller for the plant which satisfies the following two criteria for the system while maintaining closed-loop stability:

1.**Regulation** : The outputs are independent of the disturbances affecting the system.

2.**Tracking** :The outputs asymptotically track a referenced input signal applied to the system.

The controller's objective is to maintain a constant linear speed in robot's motion in the presence of disturbances. In general, robot's motion can be regulated by either changing the normal force F_N exerted on the pipe's wall via robot's wheels, changing active wheels' inclination angle δ offline, or by changing the input voltage provided to the DC motor on fly. The latter is adopted as the control variable.

5.2 Fuzzy Logic Control : An Overview

Recently, researchers have been exploiting *Artificial Intelligence* (AI) techniques to address the following two major issues where conventional control techniques still require improvement:

- Accuracy of nonlinear system modeling;

- The accommodation of plant dynamics;

The AI applications in the design and implementation of automatic control systems have been broadly described as "intelligent control". Such decision-making is inevitably autonomous and should result in improved overall performance over time. In this context, a neural-network-based fuzzy logic control strategy has been adopted in our system. The rational for this selection is that a precise linear dynamic model of our pipe crawler cannot be obtained.
FLC's incorporate heuristic control knowledge in the form of "*IF-THEN*" rules and are a convenient choice when a precise linear dynamic model of the system to be controlled cannot be easily obtained.
Furthermore, FLC's have also shown a good degree of robustness in face of large variability and uncertainty in the system parameters (Wang, 1994),(Dimeo & Lee, 1995). An ANN can learn fuzzy rules from I/O data, incorporate prior knowledge of fuzzy rules, fine tune the membership functions and act as a self learning fuzzy controller by automatically generating the fuzzy rules needed (Jang, 1993). This capability of the NN was utilized to form an FL-based controller based on data obtained via Human-In-The-Loop (HITL) simulator.

5.2.1 Structure of the FLC

The rule-base of the proposed FLC contains rules of first order TSK type (Takagi & Sugeno, 1985). In our proposed FLC the two inputs to the controller are *error in linear velocity of the robot* $e(t)$ and the *rate of change in the error* $\dot{e}(t)$ as follows:

$$\begin{cases} e(t) &= \dot{Z}_{set} - \dot{z}(t); \\ \dot{e}(t) &= -\ddot{z}(t); \end{cases} \tag{21}$$

where "$\dot{Z}_{set}$" is the set-point in velocity. The controller output is the voltage applied to the DC motor of the hub, namely $v(t)$. The rationale for this selection of the input variables is that, intuitively speaking, human makes a decision about the value of $v(t)$ based on a visual feedback (detailed under human-in-the-loop simulator) of the change of the velocity of the robot (i.e. $e(t)$) and the rate of this change (i.e. $\dot{e}$(t)). This FLC adjusts the control variable, namely the input voltage provided to the hub's actuator in order to maintain a constant speed in the robot when subjected to flow disturbances.
The structure of ANFIS model implemented is based on :

- A first order TSK fuzzy model where the consequent part of the fuzzy *IF-THEN* rules is first order in terms of the premise parameters;
- To performs fuzzy "AND", algebraic "minimum" is manipulated as the *T-norm* ;
- To performs fuzzy "OR", algebraic "maximum" is manipulated as the *T-norm* ;
- Three sets of *product-of-two-sigmoidal* MF's on each input were implemented.

These MF's are depicted in Fig. 4 and are represented by :

$$f(x;\mathbf{q}) = \frac{1}{1+e^{-a_1(x-c_1)}} \times \frac{1}{1+e^{-a_2(x-c_2)}} \tag{22}$$

where $\mathbf{q} = [a_1, a_2, c_1, c_2]$.

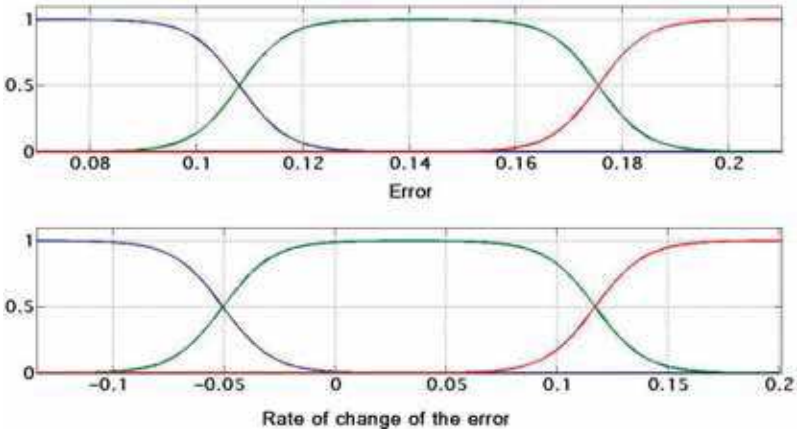

Fig. 4. Membership functions on the two inputs of the system : error and the rate of change in error before tuning.

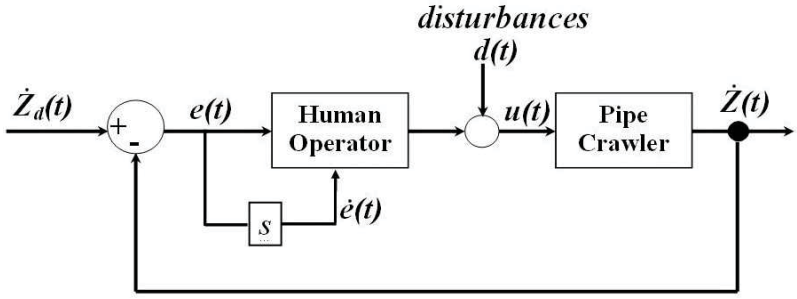

Fig. 5. Closed-loop system of the HITL simulator.

5.2.2 Human-In-the-Loop Simulator (HITL)

A real-time virtual reality HITL simulator was designed. Data acquired via this simulator was employed for training the ANFIS. The operator learns to control the velocity of the pipe crawler when subjected to flow disturbances, in the Human-Machine Interface (HMI) designed for this purpose. Fig. 5 shows the closed-loop system modeled in the HITL simulator. In this research we replace the "human operator" of the closed-loop with a stand-alone FLC whose parameters are tuned using the data acquired from the human operator, as depicted in Fig. 6

The disturbance on the system is simulated in the form of step changes in the flow velocity in the pipe. A snapshot of the HMI is given in Fig. 7. In this figure, $\dot{z}(t)$ and $\dot{Z}_{set}$ are depicted on top with a solid and a dashed line, respectively. The randomly generated flow disturbance (used for training) is also shown at the bottom of the figure. We will show through simulation that the controller tuned based on this type of disturbance is capable of rejecting different disturbances such as sinusoidal as well.

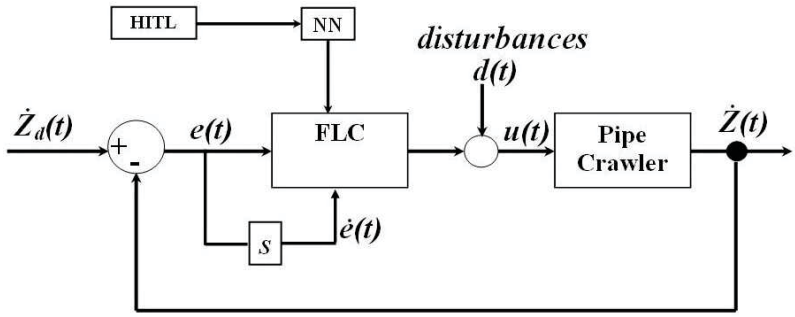

Fig. 6. FLC-based closed-loop system.

5.2.3 Acquiring Real-Time Data

The simulink model used for this purpose is depicted in Fig. 8. The disturbance in form of flow velocity and also the open-loop control signal in form of voltage (controlled by the trainee subject as explained below) are applied to the simulated system and the required data for training ANFIS (i.e. applied voltage $v(t)$, error $e(t)$ and the rate of change of error $\dot{e}(t)$) are captured and saved for manipulation in ANFIS. Also, the scope is the aforementioned HMI as in Fig. 7. A joystick was used as the *haptic device* to control the voltage applied to the DC motor actuator in the simulation environment and also experiment. The operator can continuously monitor the robot motion in real-time to correct its course of motion by varying the voltage provided to the motor.The objective is to make $\dot{z}(t)$ follow $\dot{Z}_{set}$ closely and consequently minimize the error.

Following the above procedure, we asked our trainee to accomplish the control task in the presence of step flow disturbance. The trainees go through a few trials in order to become an expert and the data provided by them can be used for training our ANFIS. The data acquisition time was set at $40s$ for the trainee to have enough time, between each of the four jumps in the flow velocity, to bring the system back to its set-point.

5.3 ANFIS Architecture

Here we elaborate on the ANFIS structure adopted in the proposed servomechanism control problem.

As explained previously (see section 5.2.1) there are three MF's on each input which yield a rule base with nine fuzzy if-then rules of first order TSK type (Turing, 1950).

$$\textit{Rule \#}i : \text{IF } e(t_h) \text{ is } A_{j1} \text{ and } \dot{e}(t_h) \text{ is } A_{j2} \text{ THEN } v_i = p_i e(t_h) + q_i \dot{e}(t_h) + r_i$$

where $i = \{1,\ldots,9\}$ is the rule number, $\{e(t_h),\dot{e}(t_h)\}$ are the numerical values of the error inputs at sampling time t_h and A_{jk}'s are linguistic variables (i.e. $\{$ *NEGATIVE , ZERO , POSITIVE* $\}$). Also $j = \{1,2,3\}$ is the node number and $k = 1,2$ is the indicator of the input (″1″ referring to a linguistic variable on ″e″ and ″2″ referring to a linguistic variable on ″$\dot{e}$″) .

The corresponding equivalent ANFIS structure is shown in Fig. 9. The node functions in each layer are of the same family.

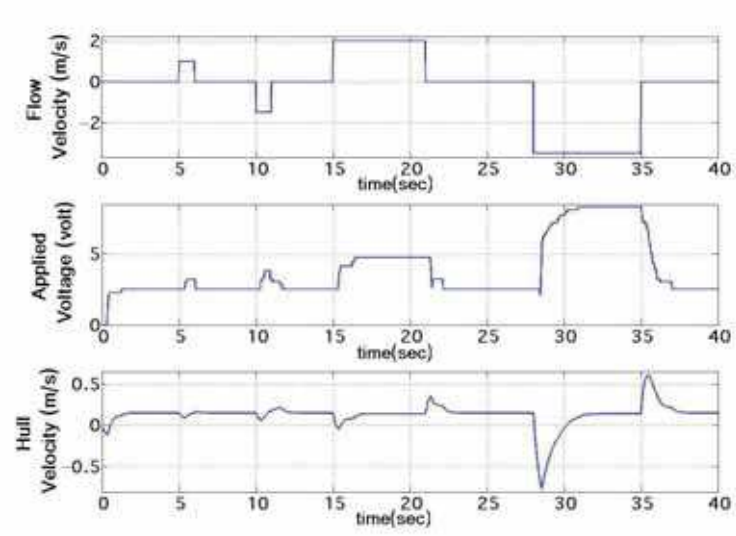

Fig. 7. A snapshot of the HMI used in this paper.

5.3.1 Hybrid Learning Rule

The architecture of ANFIS shows that the output can be expressed as: (Ghafari et al., 2006):

$$output = F(\vec{I}, S) \tag{23}$$

where $\vec{I}$ is the set of input variables S in the set of parameters. There will exist an identity function H such that the composite of $H \circ F$ is linear in some of the elements of consequent parameters S, then these elements can be identified by the Least Squared Estimation (LSE). More formally, if the parameter set S can be decomposed into two sets as:

$$S = S_1 \oplus S_2 \tag{24}$$

where $\oplus$ represents direct sum, such that $H \circ F$ is linear in the elements of S_2, then upon applying H to (23), we have:

$$H(output) = H \circ F(\vec{I}, S) \tag{25}$$

which is linear in the elements of S_2. Hence, given values of premise parameters S_1, we can plug P training data into (25) and obtain a matrix equation :

$$\mathbf{AX} = \mathbf{B} \tag{26}$$

where $\mathbf{X}$ is a vector of unknown parameters in S_2, and $\mathbf{A}$ and $\mathbf{B}$ are the set of inputs and outputs, respectively. Let $|S_2|$=M, then the dimensions of $\mathbf{A}$, $\mathbf{X}$ and $\mathbf{B}$ are $P \times M$, $M \times 1$ and $P \times 1$, respectively. As the number of training data P is usually greater than the number of linear parameters M, a least squared estimate is used to seek $\mathbf{X}$. On the other hand, the error measure for the *p-th* ($1 \leq p \leq P$) training data can be defined as the sum of squared errors:

$$E_p = \sum_{m=1}^{\#(L)} (T_{m,p} - O_{m,p}^{L})^2 \tag{27}$$

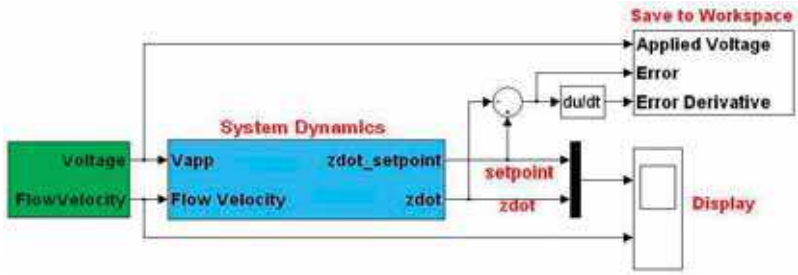

Fig. 8. Simulink model used for data acquisition.

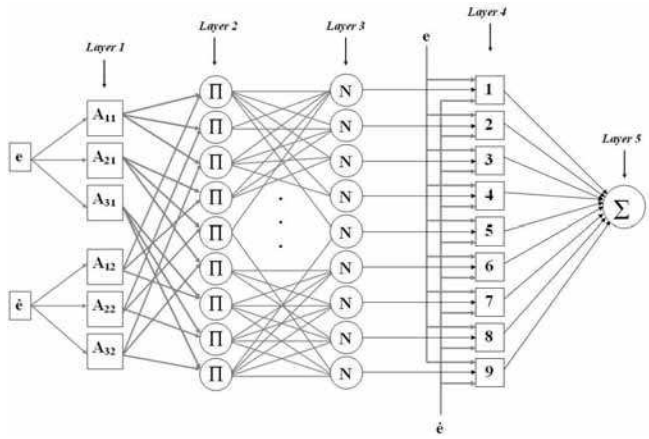

Fig. 9. The ANFIS structure adopted in this work.

where $T_{m,p}$ is the *m-th* component of the *p-th* target output vector, and $O^L_{m,p}$ is the *m-th* component of actual output vector produced by the presentation of the *p-th* input vector. Therefore, the overall error measure is equal to $E = \Sigma E_p$ and the derivative of the overall error measure E with respect to the premise parametes α is:

$$\frac{\partial E}{\partial \alpha} = \sum_{p=1}^{P} \frac{\partial E_p}{\partial \alpha} \tag{28}$$

The updated formula for the premise parameters α is :

$$\Delta\alpha = -\eta \frac{\partial E}{\partial \alpha} \tag{29}$$

where:

$$\eta = \frac{k}{\sqrt{\sum_\alpha (\frac{\partial E}{\partial \alpha})^2}} \tag{30}$$

is the learning rate for α and k is the step size and can be varied to change the speed of convergence.

5.3.2 Hybrid Learning Algorithm

Given the values of the premise parameters, the overall output of the proposed type-3 ANFIS structure can be expressed as a linear combination of the consequent parameters, i.e. the output v can be expressed as :

$$\begin{aligned} v &= \sum_{i=1}^{9} \left(\frac{w_i v_i}{\sum_{i=1}^{9} w_i} \right) \\ &= \sum_{i=1}^{9} \left((\bar{w}_i e) p_i \right) + \sum_{i=1}^{9} \left((\bar{w}_i \dot{e}) q_i \right) + \sum_{i=1}^{9} \left((\bar{w}_i) r_i \right) \end{aligned} \tag{31}$$

which is linear in terms of the consequent parameters $\{p_i, q_i, r_i\}$.

a) Forward Pass : In the forward pass of the hybrid learning algorithm, the node outputs go forward till layer 4 where the consequent parameters are identified by the *Least Square Estimate (LSE)* from (26).

a) Backward Pass : In the backward pass, the error rates of each node output propagate from the output end toward the first layer, where now the premise parameters are updated by the gradient descent using (29).

Table 2 summarizes the activities in each path. This hybrid learning algorithm is shown to efficiently obtain the optimal premise and consequent parameters during the learning process.

	Forward Pass	**Backward Pass**
Premise Parameters	Fixed	Gradient Descent
Consequent Parameters	LSE	Fixed
Signals	Node Outputs	Error Rates

Table 2. The hybrid learning procedure for ANFIS in two passes (Jang, 1993)

5.3.3 Tuning the FLC using ANFIS

In order to tune parameters of both the linguistic variables' membership functions $\mu_{A_{jk}}(x_k)$ (i.e. the set $\{a_1, a_2, c_1, c_2\}$ as in (22)) and the parameters of the rules' consequents (i.e. $\{p_i, q_i, r_i\}$ for each rule i) we used the acquired data (see section 5.2.3) based on $\{e(t), \dot{e}(t)\}$ as inputs to the controller and the DC motor voltage $v(t)$ as the output of the system. In other words, using ANFIS, the objective is to find a relationship between the inputs and output of the controller of the form $v(t) = k_1 e(t) + k_2 \dot{e}(t) + k_3$ for each rule i. One can readily conclude by referring to (31) that :

$$k_1 = \sum_{i=1}^{9} w_i p_i \quad ; \quad k_2 = \sum_{i=1}^{9} w_i q_i \quad ; \quad k_3 = \sum_{i=1}^{9} w_i r_i$$

For this purpose, each trainee accomplishes the control task for 4000 time steps or 40 seconds in each trial (sampling time was set at $\delta t = 0.01 sec$). From each training run, 2000 data points were randomly selected to tune the FLC using ANFIS. After having been trained, ANFIS was tested with the remaining 2000 sampled data for verification.

6. Simulation and Experimental Results

6.1 Simulation Results

MATLAB VR2008a together with *SIMULINK*, the *Fuzzy Logic Toolbox* and *WinCon V5.0* from Quanser (Quanser, 2009) were used for real-time simulation of our proposed system. The control objective was to maintain a pre-set constant linear speed $\dot{Z}_{set}$ while moving the robot inside a vertical pipe in the presence of hydrodynamic forces due to flow. The SIMULINK model of the feedback-loop with the proposed FLC is shown in Fig. 10.

Fig. 10. Closed-loop system using stand-alone FLC used in simulation.

6.1.1 External Disturbance Models

Two flow disturbance models were used in the simulation environment : (1) *step* changes and (2) *sinusoidal* changes in flow velocity as depicted on top of Fig. 11.

A variety of simulations were conducted based on the classical PID and also the stand-alone

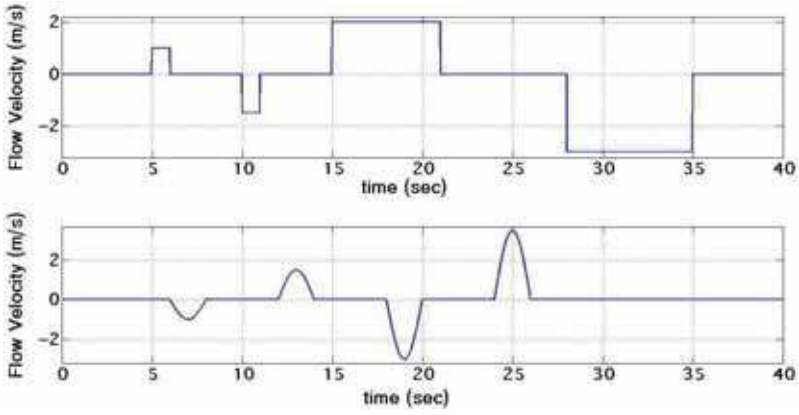

Fig. 11. Flow disturbance models used in simulation.

intelligent controller (FLC based on ANFIS), both of which were tested in a closed-loop system in the presence of the two aforementioned disturbance models and $\dot{Z}_{set}\frac{m}{s} = \{0.10, 0.15, 0.30\}$.

6.1.2 PID Control

The tests were carried out with a classical PID controller of the form :

$$u(t) = K_p e(t) + K_d \frac{de}{dt} + K_I \int_0^t e(\tau)d\tau + u_0 \tag{32}$$

The standard PID controller was designed in accordance with the Ziegler-Nichols tuning criteria (Ziegler & Nichols, 1993). The best value of gains were found to be $K_p = 20.4$, $K_i = 250$ and $K_d = 0.1285$ for proportional, integral and derivative gains, respectively. It is noteworthy that the term u_0 in (32) is to compensate for the gravitational force applied to the robot (vertical pipe).
The PID controller was designed such that the closed-loop control system would be stable and also meet given specifications associated with the following (Ang et al., 2005):

1) Stability Robustness ;
2) Tracking performance at transient, including rise time, overshoot and settling time;
3) Regulation performance at steady state;
4) Robustness against environmental uncertainty.

The response of the closed-loop system using a classical PID controller is shown in Figs. 12 to 17.

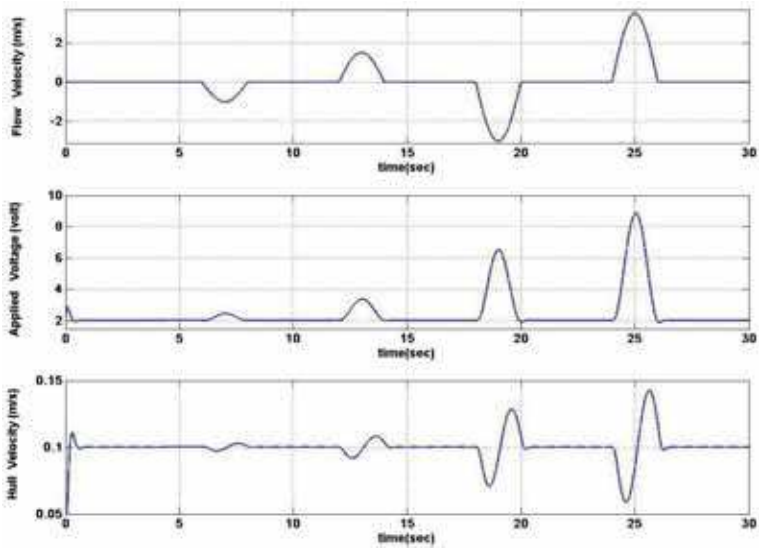

Fig. 12. Response of the closed-loop system with sinusoidal flow disturbance for $\dot{Z}_{set} = 0.10$ m/s using PID.

6.1.3 Fuzzy Logic Controller

The FLC was further optimized using ANFIS based on the following procedure:

- *Training:* A human expert was trained to accomplish the control task within a HITL real-time simulator in the presence of the flow disturbances explained above.
  One should note that for training purpose, we only used the following operating condition:
  - Step Changes in flow disturbance;
  - $\dot{Z}_{set} = 0.15 \frac{m}{s}$.

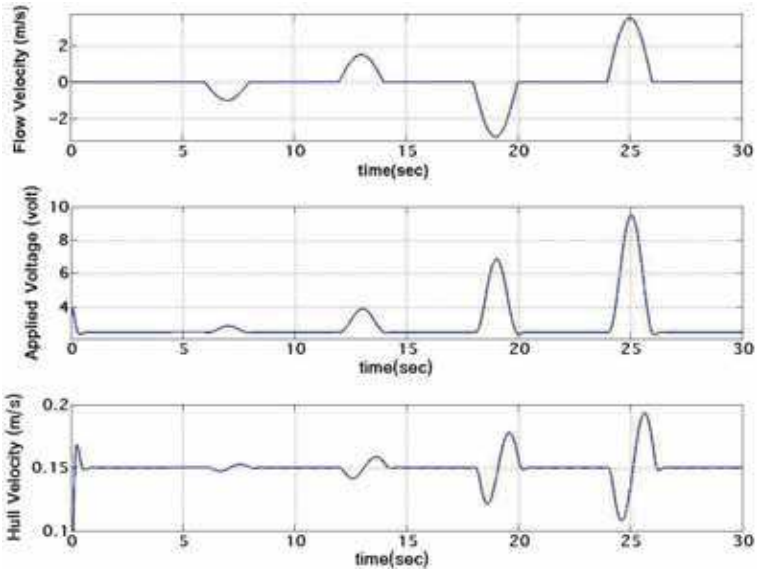

Fig. 13. Response of the closed-loop system with sinusoidal flow disturbance for $\dot{Z}_{set} = 0.15\frac{m}{s}$ using PID.

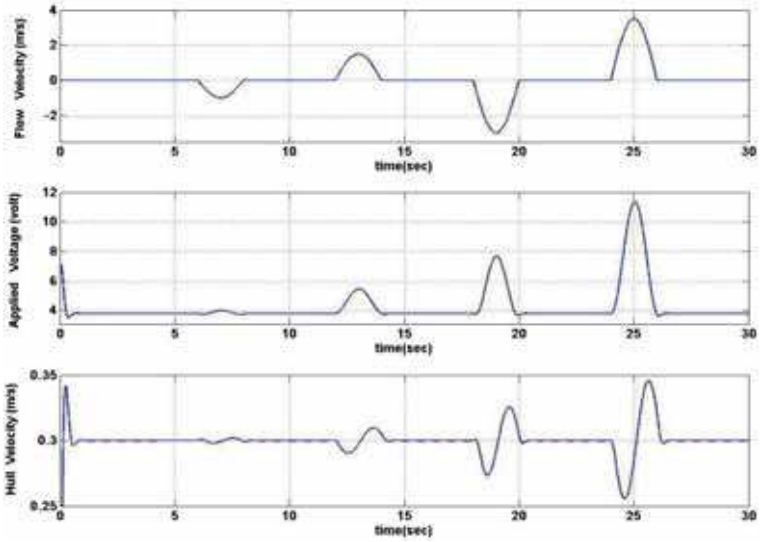

Fig. 14. Response of the closed-loop system with sinusoidal flow disturbance for $\dot{Z}_{set} = 0.30\frac{m}{s}$ using PID.

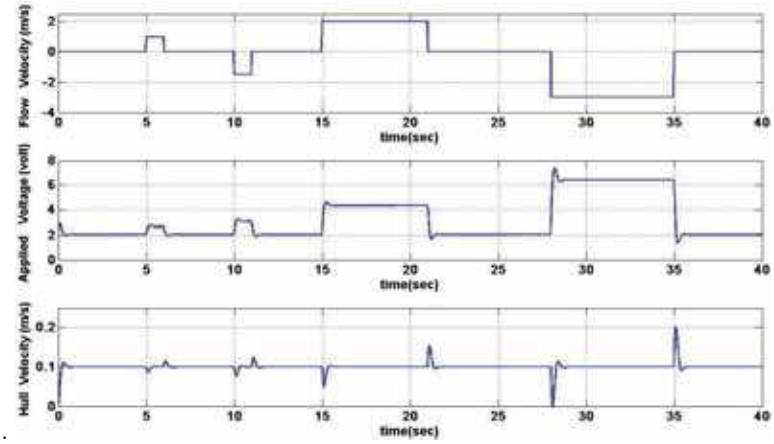

Fig. 15. Response of the closed-loop system with pulse flow disturbance for $\dot{Z}_{set} = 0.10\frac{m}{s}$ using PID.

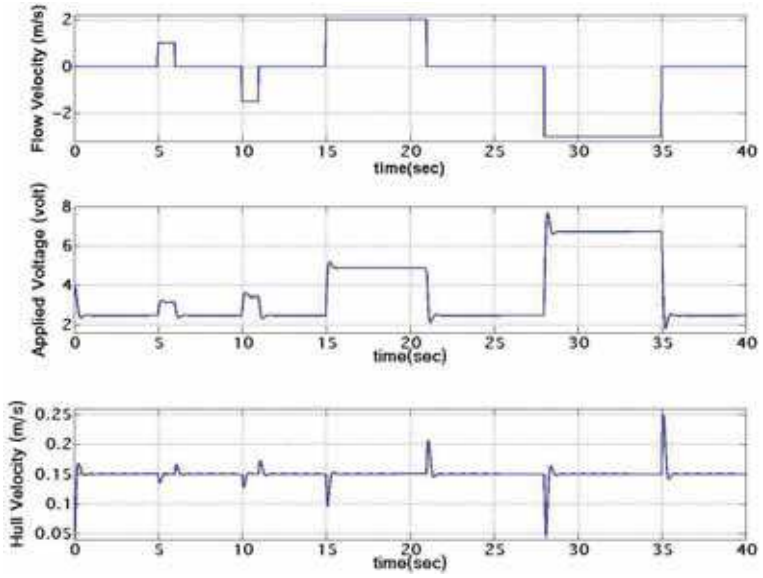

Fig. 16. Response of the closed-loop system with pulse flow disturbance for $\dot{Z}_{set} = 0.15\frac{m}{s}$ using PID.

The final training data (after a few learning trials) is shown in Fig. 18.
We will show through simulation that the FLC tuned based on ANFIS for one particular operating condition is capable of completing the servoing task under various operating

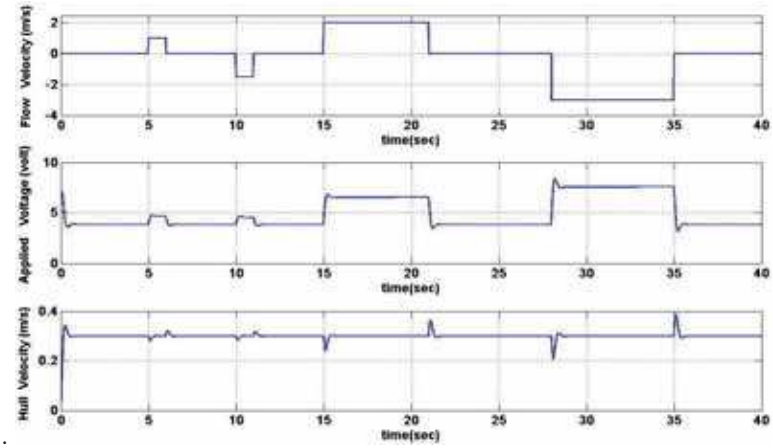

Fig. 17. Response of the closed-loop system with pulse flow disturbance for $\dot{Z}_{set} = 0.30\frac{m}{s}$ using PID.

conditions (i.e. velocity set-points and flow disturbance models, e.g. sinusoidal).

- *Tuning FLC using ANFIS :* Next we used the above acquired data to tune the parameters of the FLC in ANFIS. The inputs to the FLC were the *error,* $e(t)$ and the *rate of change of error,* $\dot{e}(t)$ (see section 5.2.1) and are presented in Fig. 19. The error tolerance in ANFIS was set at 10^{-6} and was reached after 97 epochs on average. The trend in epochs is depicted in Fig. 20. Also the modified MFs and the pertaining control surface after tuning are shown in Figs. 21 and 22, respectively.

  It is noteworthy that as the initial guess, the premise parameters are set to some (arbitrary) non-zero values as listed in Table 3 (INITIAL VALUES). Furthermore, for the consequent parameters, zero is taken as the initial guess. During the optimization process in ANFIS, both sets of values (premise and consequent parameters) are updated. The values of $\{a_l, c_l\}$ for $l = 1,2$ and $\{p_i, q_i, r_i\}$ for $i = 1,2,...,9$ after utilizing the ANFIS are listed in Tables 3 (FINAL VALUES) and 4.

The response of the closed-loop systems using optimized FLC via ANFIS is depicted in Fig. 23 to Fig. 28.

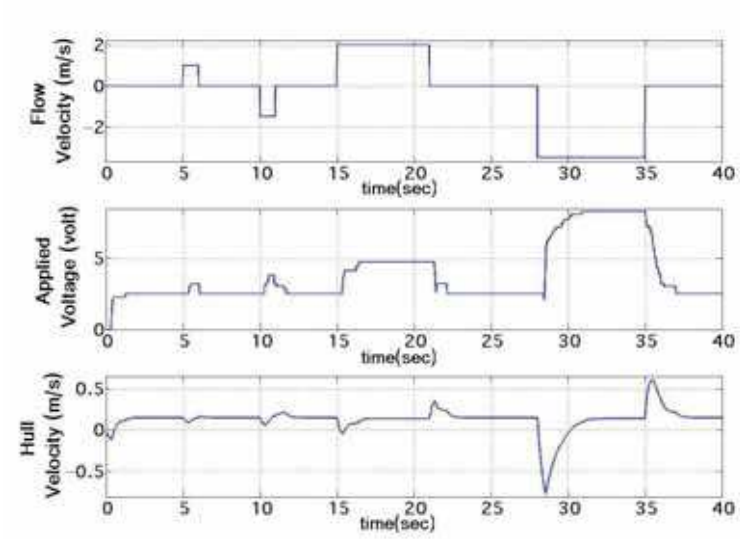

Fig. 18. The human operator's response to the flow disturbances within the HITL simulator.

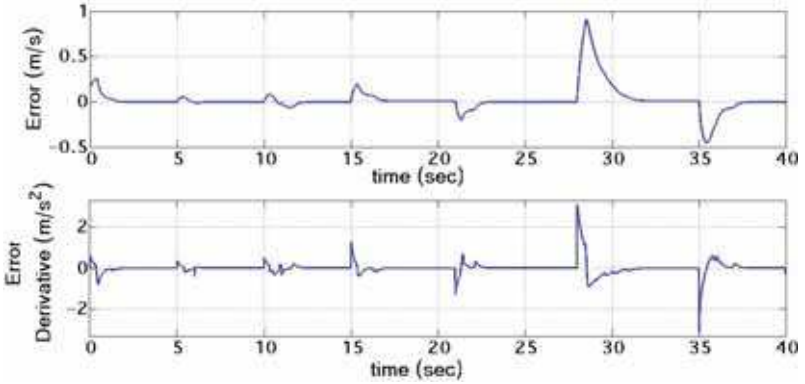

Fig. 19. Input data used in training ANFIS with step flow disturbance .

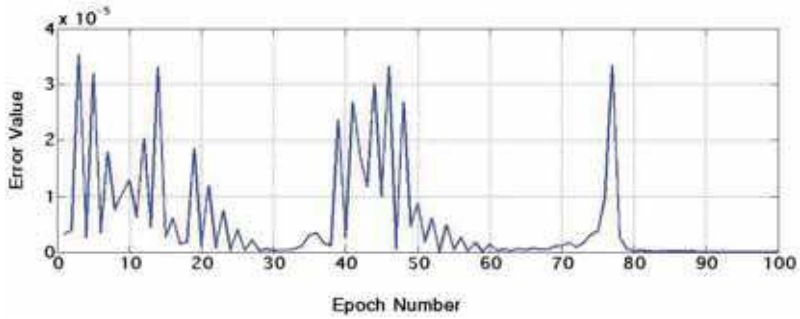

Fig. 20. Epoch evolution using ANFIS for sigmoidal membership function.

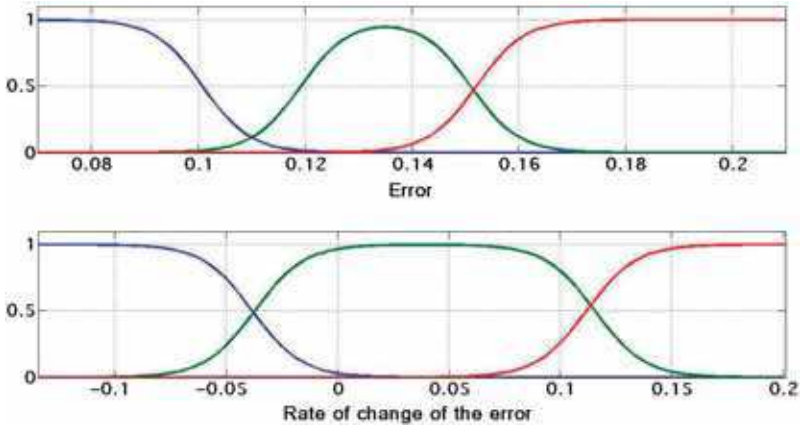

Fig. 21. MF's on the two inputs of the system : error and the rate of change in error, after tuning.

	MF	a_1	c_1	a_2	c_2
INITIAL VALUES	$\mu_{A_{11}}(e)$	222.4	0.041	-222.4	0.11
	$\mu_{A_{21}}(e)$	222.4	0.108	-222.4	0.18
	$\mu_{A_{31}}(e)$	222.4	0.1756	-222.4	0.24
	$\mu_{A_{12}}(\dot{e})$	89.33	-0.2185	-89.33	-0.05
	$\mu_{A_{22}}(\dot{e})$	89.33	-0.05	-89.33	0.12
	$\mu_{A_{32}}(\dot{e})$	89.33	0.12	-89.33	0.29
FINAL VALUES	$\mu_{A_{11}}(e)$	222.4	0.04	-222.4	0.10
	$\mu_{A_{21}}(e)$	222.4	0.12	-222.4	0.15
	$\mu_{A_{31}}(e)$	222.4	0.15	-222.4	0.24
	$\mu_{A_{12}}(\dot{e})$	89.33	-0.2185	-89.33	-0.03
	$\mu_{A_{22}}(\dot{e})$	89.33	-0.04	-89.33	0.12
	$\mu_{A_{32}}(\dot{e})$	89.33	0.1118	-89.33	0.29

Table 3. The initial value of the premise parameters.

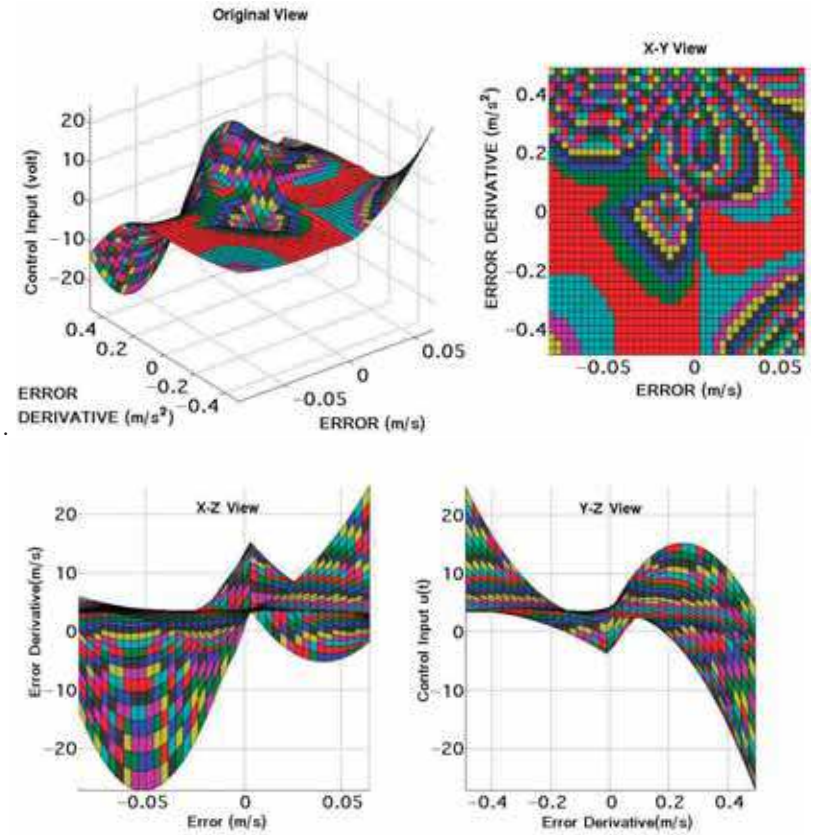

Fig. 22. Control surface of the FLC using three product-of-sigmoidal MF's, four views.

i	p_i	q_i	r_i
1	2.46	2.195	2.582
2	-0.129	1.607	2.728
3	-2.274	2.49	2.849
4	-1.602	2.343	3.03
5	10.36	2.962	0.9316
6	3.308	-1.373	2.846
7	8.068	1.932	1.277
8	8.917	1.853	1.116
9	2.43	0.072	2.497

Table 4. The final value of the consequent parameters.

6.2 Experimental Results

6.2.1 Experimental Setup

The real robotic pipe crawler was placed in an empty transparent PVC pipe of 6 inches in diameter for experimentation. The controller's objective was to track the reference input in form of a time-varying linear velocity set point. The trainee attempts to maneuver the real robot so that it follows the velocity set point visually represented in real time. The same approach was followed as in simulation to tune the FLC parameters.

6.2.2 Data Acquisition for the Real System

The position and essentially the velocity of the robot inside the pipe were captured through the optical encoder mounted on the motor. This data, in turn, was fed into the processing unit (PC) through a Q4 DAQ board from Quanser (Quanser, 2009).
Using a joystick as the haptic interface, the trainee, continuously receiving visual feedback on robot's motion on the monitor screen, applies a suitable voltage to the real system so that the linear velocity of the robot $\dot{z}(t)$ follows the desired trajectory $\dot{Z}_{set}$.

6.2.3 Tuning FLC

The data of the final trial (after a few times of training) was fed into ANFIS to tune the FLC. One should note that the FLC utilized in the experimental set up holds the same structure (i.e. type and number of MF's) used in simulation. After tuning the FLC through ANFIS, two experiments were conducted with a different $\dot{Z}_{set}$ for each, where the objective was to steer the robot along the pipe while $\dot{z}(t)$ follows the set point $\dot{Z}_{set}$ closely. The results are shown in Figs. 29 and 30 along with the control signal deployed. The human-analogous controller succeeded in carrying out the servoing task.

6.3 Discussion

6.3.1 System Performance

We have shown through simulations that not only is the FLC tuned by human data capable of accomplishing the proposed servoing task, but it also posed the following three major advantages over conventional PID controllers:

i. *Response Time:* the $(5-95)\%$ rise time t_r of the closed-loop system was decreased significantly. Table 5 summarizes the results for three different velocity set-points.

$\dot{Z}_{set}\,\frac{m}{s}$	**FLC**	**PID**	**Improvement**
0.1	0.04	0.2	400%
0.15	0.047	0.180	283%
0.3	0.086	0.158	83.72%

Table 5. Comparison of rise time t_r (in *second*) between FLC and PID.

ii. *Energy Consumption:* The control signal $u(t)$ used over the course of simulation has been decreased by using the proposed FLC. Tables 6 and 7 summarize the diffenerence in energy consumption when the robot is subjected to different flow disturbance models.

iii. *Actuator Saturation :* The control signal stays well below the saturation limit, i.e. $[-12,+12]volts$ when implementing the FLC in the closed-loop system. While using the PID controller, we reach the saturation limit at high amplitude external disturbances.

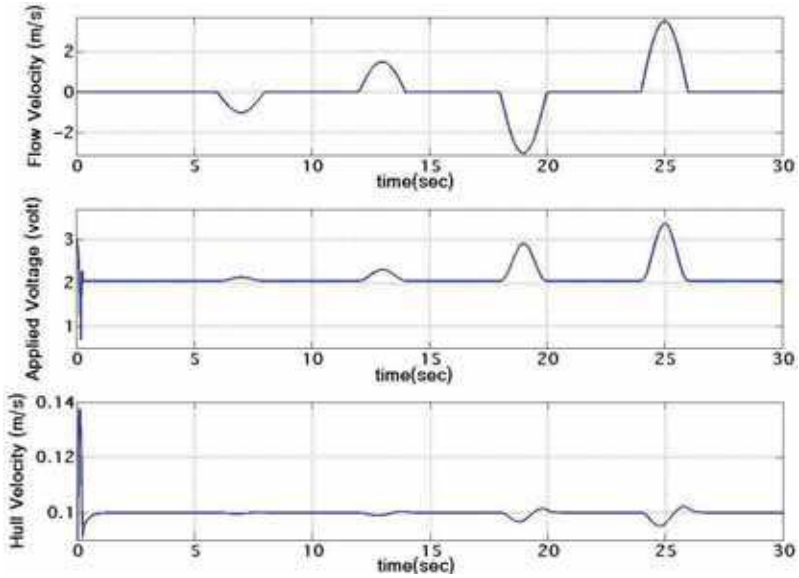

Fig. 23. Response of the closed-loop system with sinusoidal flow disturbance for $\dot{Z}_{set} = 0.10\frac{m}{s}$ using FLC.

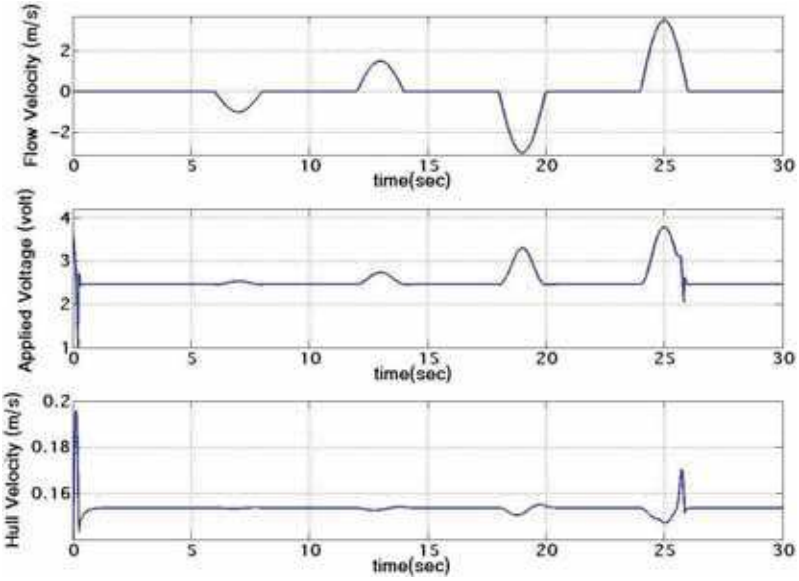

Fig. 24. Response of the closed-loop system with sinusoidal flow disturbance for $\dot{Z}_{set} = 0.15\frac{m}{s}$ using FLC.

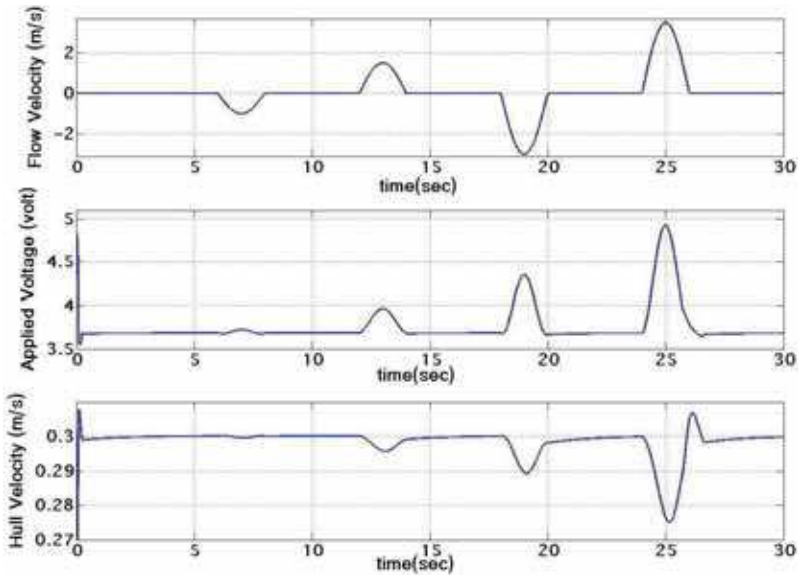

Fig. 25. Response of the closed-loop system with sinusoidal flow disturbance for $\dot{Z}_{set} = 0.30\frac{m}{s}$ using FLC.

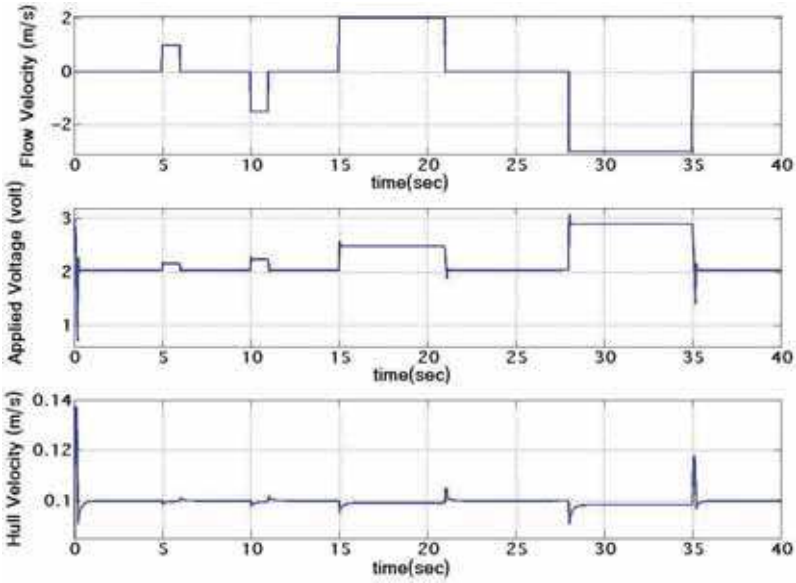

Fig. 26. Response of the closed-loop system with pulse flow disturbance for $\dot{Z}_{set} = 0.10\frac{m}{s}$ using FLC.

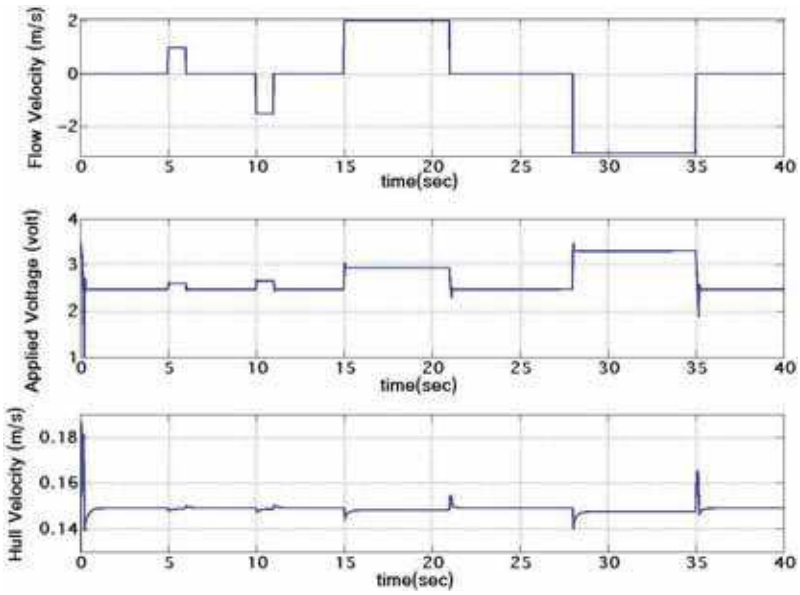

Fig. 27. Response of the closed-loop system with pulse flow disturbance for $\dot{Z}_{set} = 0.15\frac{m}{s}$ using FLC.

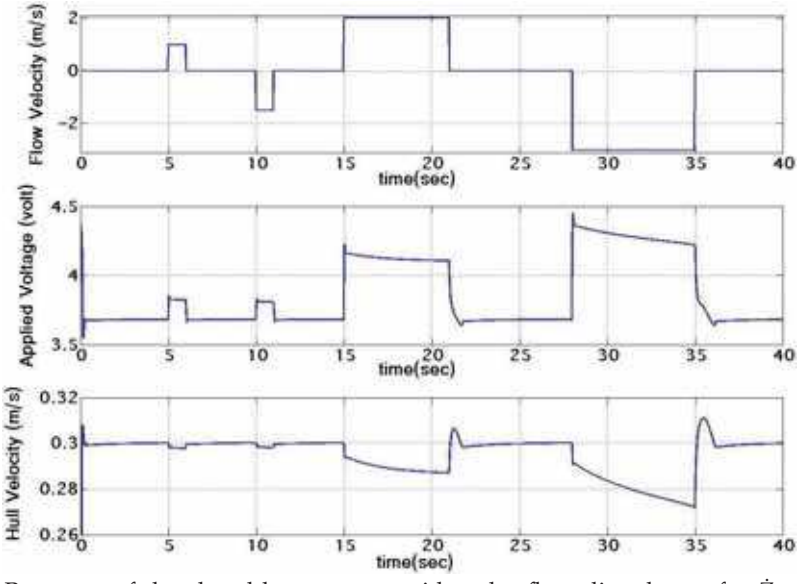

Fig. 28. Response of the closed-loop system with pulse flow disturbance for $\dot{Z}_{set} = 0.30\frac{m}{s}$ using FLC.

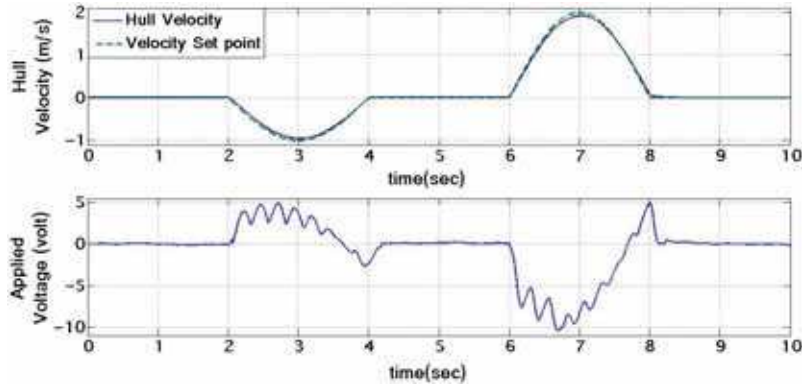

Fig. 29. Experimental results with sinusoidal reference trajectory of the velocity set point, $\dot{Z}_{set}$ using FLC.

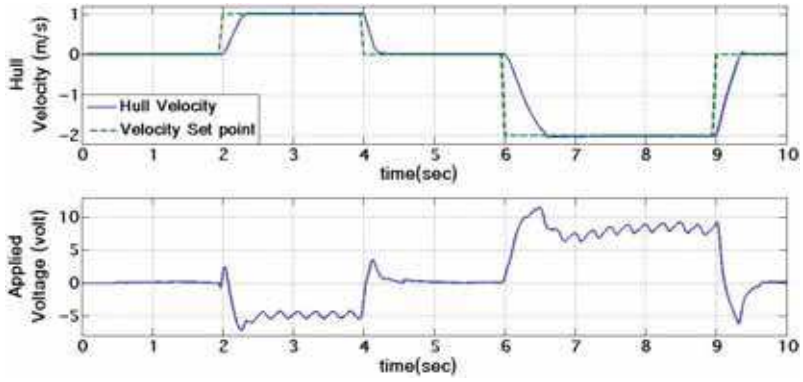

Fig. 30. Experimental results with step reference trajectory of the velocity set point, $\dot{Z}_{set}$ using FLC.

6.3.2 The Effect of MF's on the FLC Performance

As discussed previously (see section 5.2.1), we have chosen three *product-of-sigmoidal* MF's on each of the controller's inputs. This particular choice for MF's proved itself as a reasonable approximation function to relate the inputs (error and its derivative in robot's velocity) and output (voltage applied to the PMDC) , namely $u(t) = f\big(e(t),\dot{e}(t)\big)$. As an alternative, trapezoidal MF's can be also employed. Fig. 31 compares the control surface of the FLC when using *product-of-sigmoidal* and *triangular* MF's. It is noteworthy that, the same set of human data were used for tuning both systems. From Fig. 31 one can readily deduce that a system with sigmoidal MF's results in a better approximation of the relationship $u(t) = f\big(e(t),\dot{e}(t)\big)$. In technical terms, one can observe from Fig. 31 that higher control input would be required for large error in the system when using product-of-sigmoidal MF's.

The control surface on the right hand-side of Fig. 31 is not following the same expectation. The two peaks of the surface arise close to the origin (where both inputs to the system are approaching zero) and as we deviate to the edge of the surface, the control signal decreases. This

$\dot{Z}_{set}\frac{m}{s}$	FLC	PID	Improvement
0.1	83.77	94.46	12.76%
0.15	100.64	111.88	11.17%
0.3	149.13	164.75	10.47%

Table 6. Comparison of energy expenditure (*volt.s*) between FLC and PID for sinusoidal flow disturbance.

$\dot{Z}_{set}\frac{m}{s}$	FLC	PID	Improvement
0.1	90.30	127.64	41.35%
0.15	107.07	144.51	34.97%
0.3	154.06	195.72	27.04%

Table 7. Comparison of energy expenditure (*volt.s*) between FLC and PID for pulse flow disturbance.

phenomenon results in a poor performance of the closed-loop system compared to that when using product-of-sigmoidal MF's. Fig. 32 shows the control input required to servo the robot when subjected to flow disturbances using triangular and product-of-sigmoidal MF's. As can be seen from the figure, higher overshoots are observed in the FLC with triangular MF's.

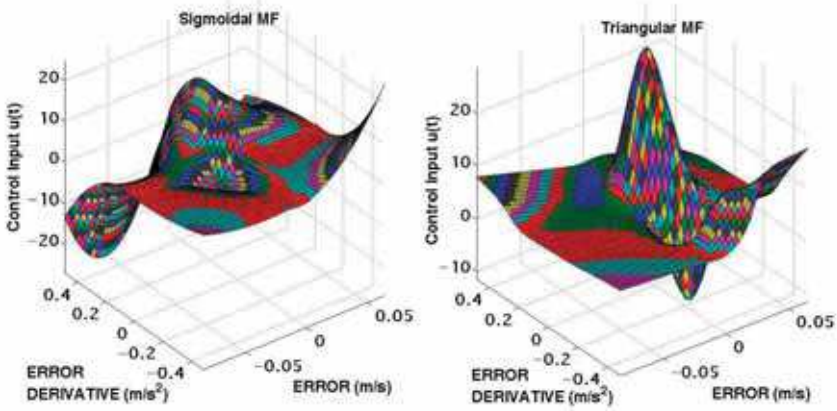

Fig. 31. Comparison between two control surfaces using triangular (left) and sigmoidal MF's (right).

7. Conclusion and Future Works

7.1 Conclusion

We addressed the design and development of a pipe crawler for water pipe inspection along with the detailed derivation and analysis of its governing dynamics equations. Also we implemented a new method for tuning the parameters of a Fuzzy-Logic based controller to regulate

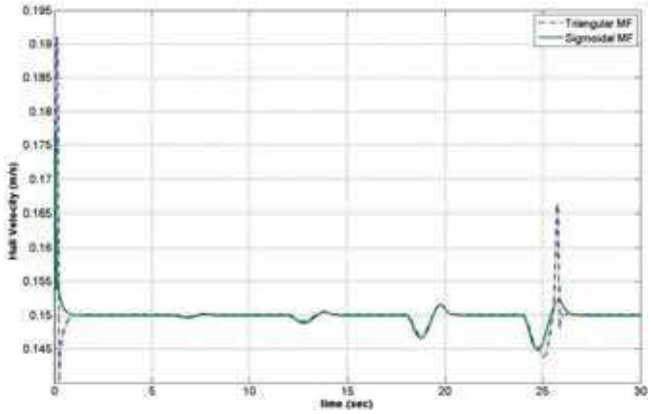

Fig. 32. Compariosn between the response of the closed-loop system using FLC with triangular and sigmoidal MF's.

the pipe crawler's velocity. The controller was designed based on a TSK model whose parameters were tuned using ANFIS. This was carried out by incorporating human analogous control strategy, obtained via a real-time HITL virtual reality simulator, into the ANFIS composition. It was shown that the proposed controller, tuned based on a specific operating condition, was capable of performing the velocity control task under various unrehearsed operating conditions as well. The controller was implemented in both simulation and experiments. It was shown that the proposed FLC outperformed a conventional PID controller.

7.2 Future Work

The future work is twofold: (1) developing a Hardware-In-the-Loop (HIL) simulation system, as depicted in Fig. 33, to control the motion of the robot when located in an empty pipe (or duct) in a dry lab where a motorized flow simulator, mechanically connected to the robot crawler via a force coupling device, will be employed to simulate the effect of hydrodynamic forces exerted on the robot as it were moving inside a live pipe, and (2) using a force/vision haptic interface for HITL control. The haptic device used in data acquisition was a regular joystick commonly used in video games. In this way, the output limitation affects the precision of human action over the course of control task. With a specialized force/vision feedback control interface, the operator will be able to control the robot motion more accurately, and consequently the optimized human analogous FLC would yield better results.

8. References

Ang, K., Chong, G., Li, Y., Ltd, Y. & Singapore, S. (2005). PID control system analysis, design, and technology, *IEEE transactions on control systems technology* **13**(4): 559–576.

Bradbeer, R., Harrold, S., Luk, B., Li, Y., Yeung, L. & Ho, H. (2000). A mobile robot for inspection of liquid filled pipes, *Workshop on Service Automation and Robotics, City University of Hong Kong*.

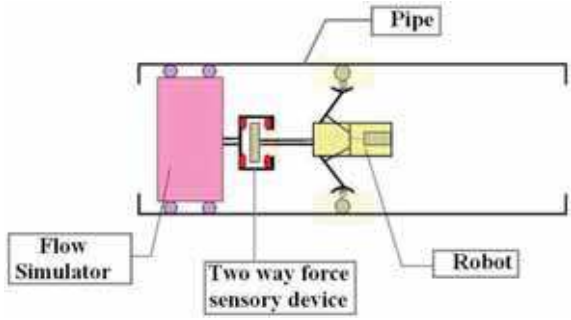

Fig. 33. The proposed HIL simulation system.

Chaudhuri, T., Hamey, L. & Bell, R. (1996). Historical Perspective:" From Conventional Control to Autonomous Intelligent Methods", *IEEE CONTROL SYSTEMS MAGAZINE* **16**: 78–87.

Dimeo, R. & Lee, K. (1995). Boiler-turbine control system design using a genetic algorithm, *IEEE Transaction on Energy Conversion* **10**(4): 752–759.

Eiswirth, M., Frey, C., Herbst, J., Jacubasch, A., Held, I., Heske, C., Hötzl, H., Kuntze, H., Kramp, J., Munser, R. et al. (2001). Sewer assessment by multi-sensor systems, *IWA 2nd World Water Congress*, pp. 15–19.

Ghafari, A., Meghdari, A. & Vossoughi, G. (2006). Intelligent Control of Powered Exoskeleton to Assist Paraplegic Patients Mobility using Hybrid Neuro-Fuzzy ANFIS Approach, *IEEE International Conference on Robotics and Biomimetics, 2006. ROBIO'06*, pp. 733–738.

Glass, S., Levesque, M., Engels, G., Klahn, F. & Fairbrother, D. (1999). UNDER-WATER ROBOTIC TOOLS FOR NUCLEAR VESSEL AND PIPE EXAMINATION, *Framatome ANP, Lynchburg Virginia* .

Griffiths, G. (2003). *Technology and applications of autonomous underwater vehicles*, CRC Press.

Grigg, N. (2006). Assessment of Water Distribution Pipes, *Infrastructure Systems* **12**(3): 147–153.

Gummow, R. & Eng, P. (2000). Corrosion Control of Municipal Infrastructure Using Cathodic Protection, *Materials Performance* .

Horodinca, M., Doroftei, I., Mignon, E. & Preumont, A. (2002). A simple architecture for in-pipe inspection robots, *Int. Colloquium on Mobile and Autonomous Systems*, Vol. 10, pp. 25–26.

Hunt, K., Sbarbaro, D., Żbikowski, R. & Gawthrop, P. (1992). Neural networks for control systems: a survey, *Automatica (Journal of IFAC)* **28**(6): 1083–1112.

Jang, J. (1993). ANFIS: Adaptive-network-based fuzzy inference system, *IEEE transactions on systems, man, and cybernetics* .

Koji, K. (1999). Underwater inspection robot–AIRIS 21, *Nuclear Engineering and Design(Switzerland)* **188**(3): 367–371.

Kulpate, C. (2006). Design and development of a stereo scanner for condition assessment of water pipes, *Technical Report UR/CSIR-01-2006*, University of Regina.

Lee, C. (1990). Fuzzy logic in control systems: fuzzy logic controller. II, *IEEE Transactions on systems, man and cybernetics* **20**(2): 419–435.

Mamdani, E. et al. (1974). Application of fuzzy algorithms for control of simple dynamic plant, *Proc. Iee* **121**(12): 1585–1588.

Miwa, Y., Satoh, S. & Hirose, N. (2002). Remote-Controlled Inspection Robot for Nuclear Facilities in Underwater Environment, *Conference: 10. international conference on nuclear engineering-ICONE 10, Arlington-Virginia (United States), 14-18 Apr 2002*.

Nauck, D., Klawonn, F. & Kruse, R. (1997). *Foundations of neuro-fuzzy systems*, John Wiley & Sons, Inc. New York, NY, USA.

Nguyen, T., Yoo, H., Rho, Y. & Kim, S. (2001). Speed control of PIG using bypass flow in natural gas pipeline, *IEEE International Symposium on Industrial Electronics, 2001. Proceedings. ISIE 2001*, Vol. 2.

Nickols, F., Bradbeer, R. & Harrold, S. (1997). An ultrasonically controlled autonomous model submarine operating in a pipe environment, *Proceedings of 4th International Conference on Mechatronics and Machine Vision in Practice,(M 2 VIP97)*, pp. 142–147.

Quanser (2009). Consulting co., `http://www.quanser.com`.

Ratanasawanya, C., Binsirawanich, P., Yazdanjo, M., Mehrandezh, M., Poozesh, S., Paranjape, R. & Najjaran, H. (2006). Design and Development of a Hardware-in-the Loop Simulation System for a Submersible Pipe Inspecting Robot, *Electrical and Computer Engineering, 2006. CCECE'06. Canadian Conference on*, pp. 1526–1529.

Roh, S. & Choi, H. (2005). Differential-drive in-pipe robot for moving inside urban gas pipelines, *IEEE Transactions on Robotics* **21**(1): 1–17.

Shiho, M., Horioka, K., Inoue, G., Onda, M., Leighty, W., Yokoo, K., Ono, S., Ohashi, K. & Hirata, M. (2004). Proposal for Environmental Observation System for Large Scale Gas Pipeline Networks Using Unmanned Airship, *AIP Conference Proceedings*, Vol. 702, p. 522.

Takagi, T. & Sugeno, M. (1985). Fuzzy identification of systems and its applications to modeling and control, *IEEE transactions on systems, man, and cybernetics* **15**(1): 116–132.

Turing, A. (1950). Computing machinery and intelligence, *Mind* **59**(236): 433–460.

Wang, L. (1993). Stable adaptive fuzzy control of nonlinear systems, *IEEE Transactions on Fuzzy Systems* **1**(2): 146–155.

Wang, L. (1994). *Adaptive fuzzy systems and control: design and stability analysis*, Prentice-Hall, Inc. Upper Saddle River, NJ, USA.

Wang, L. & Mendel, J. (1992). Fuzzy basis functions, universal approximation, and orthogonalleast-squares learning, *IEEE Transactions on Neural Networks* **3**(5): 807–814.

Zadeh, L. (1973). Outline of a new approach to the analysis of complex systems and decision processes, *IEEE Transactions on Systems, Man, and Cybernetics* **3**: 28–44.

Ziegler, J. & Nichols, N. (1993). Optimum settings for automatic controllers, *Journal of dynamic systems, measurement, and control* **115**: 220.

APPENDIX

A. Dynamics Model of the Proposed Pipe Inspecting Robot (Kinetic Energy of the Robot's Wheel)

In order to derive the dynamics model of our proposed system, three coordinate frames, as shown in Figure 3, are taken into consideration which are as follows:

- Inertial reference system - This is the earth-fixed coordinate system defined by a right-handed, orthogonal X_i, Y_i, Z_i coordinate frame. The Z_i axis is parallel to the pipe's centerline and is pointed upward. The X_i and Y_i directions and the location of the origin can be selected arbitrarily (within the requirement of orthogonality). The inertial frame is denoted by letter i.

- Body-fixed coordinate frame - This is the body-fixed coordinate system that is defined by a right-handed, orthogonal coordinate system attached to the robot's hull. Its origin lies on the hull's centre of gravity. The Z_B axis is set parallel to the Z_i and is pointed upward. The X_B and Y_B axes remain perpendicular to the Z_B axis within the requirement of orthogonality. The body-fixed frame is denoted by letter B.
- Wheel-fixed coordinate frame - This is the right-handed orthogonal reference frame fixed to the wheel with its origin located on the intersection point between the Y_B axis and the wheel center. The Z_W axis is perpendicular to the wheel's plane pointing towards the vehicle's direction of motion. It makes an angle of δ with respect to the the Z_B axis. The X_W and Y_W axes remain perpendicular to the Z_W axis within the requirement of orthogonality. The wheel-fixed frame is denoted by letter W.

One should note that the extension of robot's arms is not considered in the dynamics model for simplicity. Therefor distance b remains at constant . Transformations from the wheel- and body-fixed coordinate frames to the inertial reference frame are described here. The general orientation of the wheel-fixed frame (hereinafter called wheel frame) represented in the inertial frame can be utilized through a number of successive rotations called Euler Angles. The relative rotation between the wheel frame and inertial frame can be represented as follows:

$$\mathbf{R}_W^i = \mathbf{R}_B^i \times \mathbf{R}_W^B \tag{A-1}$$

where " $\times$ " denotes matrix product and $\mathbf{R}_B^i$ and $\mathbf{R}_W^B$ are as listed below:

$$\mathbf{R}_B^i = \begin{bmatrix} C_\phi & -S_\phi & 0 \\ S_\phi & C_\phi & 0 \\ 0 & 0 & 1 \end{bmatrix} \tag{A-2}$$

$$\mathbf{R}_W^B = \begin{bmatrix} C_\delta C_\theta & -C_\delta S_\theta & S_\delta \\ S_\theta & C_\theta & 0 \\ -S_\delta C_\theta & S_\delta S_\theta & C_\delta \end{bmatrix} \tag{A-3}$$

Hence:

$$\mathbf{R}_W^i = \begin{bmatrix} C_\phi C_\delta C_\theta - S_\phi S_\theta & -C_\phi C_\delta S_\theta - S_\phi C_\theta & C_\phi S_\delta \\ S_\phi C_\delta C_\theta + C_\phi S_\theta & -S_\phi C_\delta S_\theta + C_\phi C_\theta & S_\phi S_\delta \\ -S_\delta C_\theta & S_\delta S_\theta & C_\delta \end{bmatrix} \tag{A-4}$$

In (A-1) through (A-3), ϕ, θ, and δ denote the rotational angle of the robot's body with respect to the inertial frame, the rotational angle of the wheel with respect to the body frame, and the inclination angle of the wheels, respectively. One should note that the following notation is used in long equations; $C_a = cos(a)$, and $S_a = \sin(a)$.
Total kinetic energy of each robot's wheel can be calculated as follows:

$$T_{wheel} = \frac{1}{2} m (\mathbf{v}_W^i)^T (\mathbf{v}_W^i) + \frac{1}{2} (\mathbf{!}_W^i)^T \mathbf{I}_W^i (\mathbf{!}_W^i) \tag{A-5}$$

where $\mathbf{v}_W^i$,$\mathbf{!}_W^i$, and $\mathbf{I}_W^i$, m denote the linear velocity of the origin of the wheel frame, the angular velocity of the wheel frame ,the wheel's inertial tensor all represented in the inertial frame and the wheel's mass, respectively.These terms are described below in more detail.
One can write:

$$(\mathbf{v}_W^i) = (\mathbf{v}_B^i) + (\mathbf{v}_{B,W}^i) + (\mathbf{!}_B^i) \times (\mathbf{r}_{B,W}^i) \tag{A-6}$$

where $\mathbf{v}_B^i$ denotes the velocity of the origin of the body frame represented in the inertial frame, $\mathbf{v}_{B,W}^i$ denotes the relative velocity of the wheel frame and body frame represented in the inertial frame, $\boldsymbol{!}_B^i$ denotes the angular velocity of the body frame represented in the inertial frame, and $\mathbf{r}_{B,W}^i$ denotes the vector connecting the origin of the body frame to the origin of the wheel frame represented in the inertial frame. One can readily conclude:

$$(\mathbf{v}_B^i) = \begin{bmatrix} 0 & 0 & rS_\delta\dot{\theta} \end{bmatrix}^T \tag{A-7}$$

and :

$$(\boldsymbol{!}_B^i) = \begin{bmatrix} 0 & 0 & \dot{\phi} \end{bmatrix}^T \tag{A-8}$$

With the assumption that the robot's arms are fixed, namely $b = Constant$ (see Figure 3), one can conclude: $\mathbf{v}_{B,W}^i = \mathbf{0}^T$. One can also write:

$$\begin{aligned} (\mathbf{r}_{B,W}^i) &= (\mathbf{R}_B^i)(\mathbf{r}_W^B) \\ &= (\mathbf{R}_B^i)\begin{bmatrix} 0 & b & 0 \end{bmatrix}^T \\ &= \begin{bmatrix} -bS_\phi & bC_\phi & 0 \end{bmatrix}^T \end{aligned} \tag{A-9}$$

After substituting (A-7-A-9) into (A-6), one gets:

$$\mathbf{v}_W^i = \begin{bmatrix} -bC_\phi\dot{\phi} & -bS_\phi\dot{\phi} & rS_\delta\dot{\theta} \end{bmatrix}^T \tag{A-10}$$

Correspondingly, the angular velocity of the wheel frame represented in the inertial frame can be calculated as follows:

$$(\boldsymbol{!}_W^i) = (\boldsymbol{!}_B^i) + (\boldsymbol{!}_{B,W}^i) \tag{A-11}$$

where $\boldsymbol{!}_{B,W}^i$ denotes the relative angular velocity between the wheel frame and that for the body frame represented in the inertial frame. One can write:

$$\begin{aligned} (\boldsymbol{!}_{B,W}^i) &= (\mathbf{R}_B^i)(\boldsymbol{!}_W^B) \\ &= (\mathbf{R}_B^i)\begin{bmatrix} -S_\delta\dot{\theta} & 0 & -C_\delta\dot{\theta} \end{bmatrix}^T \\ &= \begin{bmatrix} -C_\phi S_\delta\dot{\theta} & -S_\phi S_\delta\dot{\theta} & -C_\delta\dot{\theta} \end{bmatrix}^T \end{aligned} \tag{A-12}$$

By substituting (A-8) and (A-12) in (A-11) one can write:

$$\boldsymbol{!}_W^i = \begin{bmatrix} -\dot{\theta}C_\phi S_\delta & -\dot{\theta}S_\phi S_\delta & \dot{\phi} - \dot{\theta}C_\delta \end{bmatrix}^T \tag{A-13}$$

With the assumption that the wheel assembly has a symmetric mass distribution about its axis of rotation and with the assumption of small wheel's inclination angle, δ, its inertia tensor expressed in the inertial frame can be calculated as follows:

$$\mathbf{I}_W^i = \mathbf{R}_B^i \begin{bmatrix} I_{WX} & 0 & 0 \\ 0 & I_{WY} & 0 \\ 0 & 0 & I_{WZ} \end{bmatrix} (\mathbf{R}_B^i)^T \tag{A-14}$$

Where the diagonal of the inertia matrix given in (A-14) denotes the moment of inertia of the wheel around the X, Y, and Z axes of the wheel frame, respectively. One should note that $I_{WX} = I_{WY}$.

By substituting (A-10), (A-13) and (A-14) in (A-5) , one can derive the following for the kinetic energy of the angled-wheel:

$$T_{AW} = \left\{ \left(mr^2 + I_{WZ} \right) \left(\frac{bC_\delta}{b+r} \right)^2 + \left(mr^2 + I_{WX} \right) S_\delta^2 \right\} \frac{\dot{\theta}}{2} \tag{A-15}$$

One should note that the kinematics constraint of $\dot{\phi} = \left(\frac{rC_\delta}{b+r} \right) \dot{\theta}$, applicable under no slippage condition on robot wheels, was utilized to derive (A-15) as well. (A-15) can be further simplified for small inclination angles of the wheels, δ in which case one can assume; $\sin(\delta) \approx 0$ and $\cos(\delta) \approx 1$ as follows:

$$T_{AW} = \left(\frac{b}{b+r} \right)^2 \left(mr^2 + I_{WZ} \right) \frac{\dot{\theta}^2}{2} \tag{A-16}$$

Assuming the wheel as a cylinder with the radius of r and height of h , $I_{WZ} \cong \frac{mr^2}{2}$ and upon substituting in (A-16) yields:

$$T_{AW} = \frac{3}{4} \frac{mr^2 b^2}{(b+r)^2} \dot{\theta}^2 \tag{A-17}$$

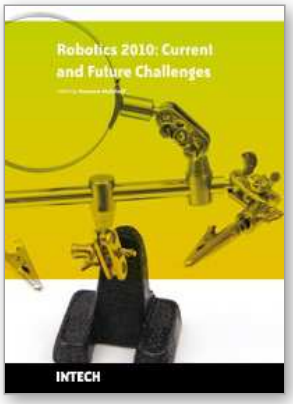

Robotics 2010 Current and Future Challenges

Edited by Houssem Abdellatif

ISBN 978-953-7619-78-7
Hard cover, 494 pages
Publisher InTech
Published online 01, February, 2010
Published in print edition February, 2010

Without a doubt, robotics has made an incredible progress over the last decades. The vision of developing, designing and creating technical systems that help humans to achieve hard and complex tasks, has intelligently led to an incredible variety of solutions. There are barely technical fields that could exhibit more interdisciplinary interconnections like robotics. This fact is generated by highly complex challenges imposed by robotic systems, especially the requirement on intelligent and autonomous operation. This book tries to give an insight into the evolutionary process that takes place in robotics. It provides articles covering a wide range of this exciting area. The progress of technical challenges and concepts may illuminate the relationship between developments that seem to be completely different at first sight. The robotics remains an exciting scientific and engineering field. The community looks optimistically ahead and also looks forward for the future challenges and new development.

InTech Europe
University Campus STeP Ri
Slavka Krautzeka 83/A
51000 Rijeka, Croatia
Phone: +385 (51) 770 447
Fax: +385 (51) 686 166
www.intechopen.com

InTech China
Unit 405, Office Block, Hotel Equatorial Shanghai
No.65, Yan An Road (West), Shanghai, 200040, China
中国上海市延安西路65号上海国际贵都大饭店办公楼405单元
Phone: +86-21-62489820
Fax: +86-21-62489821